Palaeogeography, Palaeoclimatology, Palaeoecology 534 (2019) 109281

Contents lists available at ScienceDirect

Palaeogeography, Palaeoclimatology, Palaeoecology

journal homepage: www.elsevier.com/locate/palaeo

Sulfate-controlled marine euxinia in the semi-restricted inner Yangtze Sea (South China) during the Ordovician-Silurian transition

Na Li[a], Chao Li[a,*], Junxuan Fan[b], Thomas J. Algeo[a,c,d], Detian Yan[e], Guangyou Zhu[f], Shiyong Wu[g], Shida Tang[a], Meng Cheng[a], Chengsheng Jin[a]

[a] State Key Laboratory of Biogeology and Environmental Geology, China University of Geosciences, Wuhan 430074, China
[b] School of Earth Sciences and Engineering, Nanjing University, Nanjing 210023, China
[c] State Key Laboratory of Geological Processes and Mineral Resources, China University of Geosciences, Wuhan 430074, China
[d] Department of Geology, University of Cincinnati, Cincinnati, OH 45221, USA
[e] Key Laboratory of Tectonics and Petroleum Resources of Ministry of Education, China University of Geosciences, Wuhan 430074, China
[f] Research Institute of Petroleum Exploration and Development, PetroChina, Beijing 100083, China
[g] School of Earth and Environment, Anhui University of Science & Technology, Huainan 232001, China

ARTICLE INFO

Keywords:
Wufeng Formation
Longmaxi Formation
Hirnantian glaciation
Fe speciation
Redox conditions
Sulfur isotopes

ABSTRACT

Conflicting published interpretations of marine redox conditions during the Ordovician-Silurian transition (OST) may have been linked to spatial redox heterogeneity during this interval. However, details of the pattern of redox heterogeneity and its underlying causes remain unclear. Here, we present a high-resolution geochemical study of a drillcore section (Pengye #1) from Pengshui County (Chongqing municipality, southwestern China) that was located in the semi-restricted inner Yangtze Sea during the OST. We analyzed Fe-speciation, redox-sensitive trace elements, major elements, and pyrite $\delta^{34}S$ compositions ($\delta^{34}S_{py}$) and then compared these data with published results from coeval sections at Datianba and Shuanghe in the same basin. The integrated dataset demonstrates pronounced spatiotemporal heterogeneity of redox conditions—especially the local development of euxinic conditions in the inner Yangtze Sea during the OST. Integrated data further suggest that high primary productivity and ample Fe fluxes in the inner Yangtze Sea may have depleted dissolved sulfate through microbial sulfate reduction (MSR) and subsequent pyrite formation, except in areas with enhanced sulfate supply from continental weathering or open-ocean exchange, which varied as a function of both tectonic (i.e., the regional Kwangsian Orogeny) and eustatic changes (i.e., the global Hirnantian glaciation). Limited sulfate availability thus likely prevented the development of euxinic conditions in some regions of the inner Yangtze Sea, as reflected in spatial variation of $\delta^{34}S_{py}$. Our study highlights the potential role of sulfate availability on the development of watermass euxinia in semi-restricted marginal-marine basins during the OST.

1. Introduction

The Ordovician-Silurian transition (OST) was characterized by significant climatic cooling (Saltzman and Young, 2005), culminating in a ~1.0-Myr-long glacial event during the Hirnantian Stage (445.2–443.8 Ma) (Brenchley, 1988; Kump et al., 1999; Chen et al., 2005; Dronov, 2013). This glaciation coincided with the second severest mass extinction of the Phanerozoic, marked by the loss of ~85% of marine species (Brenchley, 1988; Jablonski, 1991; Rong et al., 2007). The mass extinction occurred in two stages, the first coincident with the onset of glaciation at the beginning of the Hirnantian (base of *Metabolograptus extraordinarius* Zone), and the second coincident with the termination of glaciation in the late Hirnantian (base of *M. persculptus* Zone) (Chen et al., 2004; Wang et al., 2019). The first stage was characterized by deep losses of shallow-marine invertebrates, including plankton and benthos, as well as some deep-water organisms such as the *Foliomena* Fauna (Rong et al., 1999; Ries et al., 2009; Rasmussen and Harper, 2011). The *Hirnantia* Fauna, a distinctive shallow-marine, cold-adapted, brachiopod-dominated community with a global distribution, flourished between the two extinction events but was decimated during the second extinction pulse (Rong et al., 2002; Zhan et al., 2010).

The mechanism of the mass extinction was likely complex. The Hirnantian glaciation coincided with a drop of ~5 °C in tropical sea-surface temperatures linked to the formation of Gondwanan icesheets (Finnegan et al., 2011), applying severe temperature stress to many

* Corresponding author.
E-mail address: chaoli@cug.edu.cn (C. Li).

https://doi.org/10.1016/j.palaeo.2019.109281
Received 7 June 2019; Received in revised form 18 July 2019; Accepted 20 July 2019
Available online 29 July 2019
0031-0182/

tropical marine organisms (Yan et al., 2010). In addition, the severity of the biocrisis may have been enhanced by environmental perturbations (Algeo et al., 2016). The glaciation caused a global sea-level fall of > 70 m (Sheehan, 2001; Loi et al., 2010) with a consequent widespread loss of shallow-marine habitats (Stanley, 2010). Volcanism, which is evidenced by abundant K-bentonites and Hg enrichments in eastern North America, southeastern South China and Europe, may have played a role in regional extinctions (Huff, 2008; Su et al., 2009; Jones et al., 2017; Yang et al., 2019). However, a recent study demonstrated that Hg in Upper Ordovician strata is hosted mainly by sulfides, and that key sections show no Hg enrichment on a S-normalized basis, casting doubt on the utility of Hg as a proxy for volcanic activity during this interval (Shen et al., 2019).

Oceanic redox changes may have been a contributing factor to mass extinctions during the OST. However, both an intensification of deep-marine euxinia (Zhang et al., 2009; Hammarlund et al., 2012) and enhanced oxygenation of shallow and deep waters (Chen et al., 2004; Yan et al., 2012) have been inferred in response to Hirnantian climatic cooling and glaciation, with the latter scenario favored by Mo-isotope variations (Zhou et al., 2015; Lu et al., 2017). Recent research has demonstrated strong spatial redox heterogeneity conditions in the Neoproterozoic and early Cambrian oceans (e.g., Li et al., 2010, 2015; Jin et al., 2016; Zhang et al., 2017). Similar redox heterogeneity has been inferred for the OST in South China (Liu et al., 2016), which potentially can account for the conflicting redox observations above and, thus, is of significance for understanding marine redox controls on the end-Ordovician mass extinction event. However, details of the pattern of spatial heterogeneity in marine redox conditions and its underlying causes remain largely unclear.

The Late Ordovician inner Yangtze Sea was a hydrologically semi-restricted cratonic sea that was strongly affected by the regional Kwangsian Orogeny and global Hirnantian glaciation (Chen, 2012; Zhou et al., 2015; Liu et al., 2016). In order to investigate the relationship of redox heterogeneity to potential controls thereon, we selected three sections (Pengye #1, Shuanghe, and Datianba) from the inner Yangtze Sea that accumulated at markedly different water depths, providing an opportunity to trace the effects of glacio-eustatic changes and regional orogeny on marine redox conditions. First, we carried out a multiproxy study of the Pengye #1 drillcore using Fe-speciation, redox-sensitive trace element (Mo, U, V), major element, and pyrite S-isotope ($\delta^{34}S_{py}$) data. Then, we combined these results with published data for the Shuanghe and Datianba sections (Liu et al., 2016), producing an integrated dataset that allowed us to evaluate not only redox variation but also paleoproductivity, terrigenous fluxes, and the degree of hydrographic restriction of the inner Yangtze Sea during the OST. Our study provides new insights into the role of sulfate availability on the development of watermass euxinia in semi-restricted marginal-marine basins as well as into the causes of the end-Ordovician biocrisis.

2. Geologic setting

2.1. Paleogeography, thermal evolution, stratigraphy and bathymetry

The South China Block was an isolated microcontinent located off the northwestern margin of Gondwana in tropical to subtropical latitudes during the Late Ordovician (Fig. 1A; Cocks, 2001; Cocks and Torsvik, 2002). The Yangtze Platform, the central part of the South China Block, was covered by a broad epicratonic sea (the Yangtze Sea) within which several basinal depocenters were located; it was bordered to the north by the open ocean and to the east by another strongly restricted basin (Fig. 1B). The Yangtze Sea was divided into inner and outer regions by the Hunan-Hubei Arch (or "Submerged High") (Chen, 1984). During the Late Ordovician Kwangsian Orogeny, the Cathaysia Block collided with the Yangtze Block, resulting in northwest-southeast compression that caused a deepening of the inner Yangtze Sea and uplift of some margins of the craton (i.e., the Dianqian, Jiangnan-Xuefeng, and Chengdu uplifts) and the interior Hunan-Hubei Arch (Fig. 1B–C; Wang, 1985; Faure et al., 2009; Charvet et al., 2010; Chen, 2012). As a consequence, the inner Yangtze Sea became semi-isolated from the open ocean and developed anoxic, stagnant, low-energy bottomwaters (Mu et al., 1981; Wang, 1985; Chen et al., 2004; Liu et al., 2016). Several local depressions existed within the inner Yangtze Sea, i.e., the Chuandong and Chuannan depocenters, both to the southwest of the Hunan-Hubei Arch (Liang et al., 2009; Fig. 1C).

The Pengye #1 study section and two comparative sections (Datianba and Shuanghe) were located in the inner Yangtze Sea region (Fig. 1C). The Pengye #1 drillcore (Pengshui County, Chongqing Municipality; 29°17′47″N, 108°09′39″E) was located near the Hunan-Hubei Arch/High. It was the shallowest section (see below) and the one most proximal to the open ocean according to paleogeographic reconstructions (Fig. 1C; Liang et al., 2009; L. Zhang et al., 2014). The Datianba section (Xiushan County, Chongqing Municipality; 28°27′58″N, 108°55′53″E) was located closer to the Dianqian Uplift and the tectonically active belt between the Yangtze and Cathaysia blocks, and the Shuanghe section (Changning County, Sichuan Province; 28°23′5″N, 104°53′3″E) was located in the innermost Yangtze Sea (Fig. 1C). The Pengye #1 and Datianba sections were within the broad Chuandong depocenter, whereas the Shuanghe section was near the middle of the Chuannan depocenter and, thus, was more distant from open-ocean influences.

All three sections contain the Upper Ordovician Wufeng Formation and uppermost Ordovician-lower Silurian Longmaxi Formation, both of which are dominantly graptolitic black shales with intercalations of siliceous shale and mudstone, although bioturbated shales and siltstones are common around the basin margins (Li et al., 2017b). The Guanyinqiao Bed, a carbonaceous limestone unit containing the cold-water-adapted *Hirnantia* Fauna that is sandwiched between the Wufeng and Longmaxi formations (Chen et al., 2017), is present at Shuanghe and Datianba but absent at Pengye #1 (Fig. 2). Absence of the Guanyinqiao Bed at Pengye #1 and other sections close to the Hunan-Hubei Arch (Li et al., 2012) may reflect an unconformity linked to local uplift of this area during the Late Ordovician Kwangsian Orogeny (Chen et al., 2004, 2014; Fig. 1C). All three sections underwent similar thermal histories with maximum burial temperatures of ~210–250 °C according to backstripping analyses, measurement of vitrinite reflectance, and analysis of clay minerals (Qing et al., 2009; Li et al., 2012; Nie et al., 2012; J.K. Zhang et al., 2014).

The three study sections were deposited at different water depths, which can be estimated tentatively based on several considerations. Paleogeographic reconstructions show that Pengye #1, Datianba, and other nearby sections were located on the flanks of the Hunan-Hubei Submarine High or the structural saddle connecting it with the Dianqian Uplift, hence in areas of shallow seas (Fig. 1C; L. Zhang et al., 2014). Although the Pengye #1 drillcore is too broken up at the Wufeng-Longmaxi formation contact to permit identification of unconformity-related features, such features (e.g., weathering crusts) have been recognized in other sections in this area (e.g., Sinan, Rong et al., 2011; Gaoluo, Wufeng, and Zhangjiajie, Fan et al., 2012), indicating the existence of local subaerially exposed islands within the inner Yangtze Sea (Zhang et al., 2016). In contrast to Pengye #1 and Datianba, Shuanghe was located in the middle of the Chuannan depocenter and, thus, at relatively greater water depths (Fig. 1C).

Regional variations in the *Hirnantia* Fauna are also related to water depth. Sections in the Chuannan depocenter (e.g., Shuanghe) contain a high-diversity *Hirnantia* Fauna, equivalent to BA3 (Benthic Assemblage 3) (Rong et al., 2002; Zhan et al., 2010), representing water depths of 30–60 m (Rong, 1986). On the other hand, sections from the Chuandong depocenter (e.g., Datianba and Songtao) contain a low-diversity *Hirnantia* Fauna that includes *Hirnantia aff. sagittifera* and *H. crassa incipiens*, equivalent to BA2 (Benthic Assemblage 2), representing water depths of just 10–30 m during the Hirnantian glaciation (Rong et al., 2002). Given that non-glacial eustatic elevations were 70–100 m higher

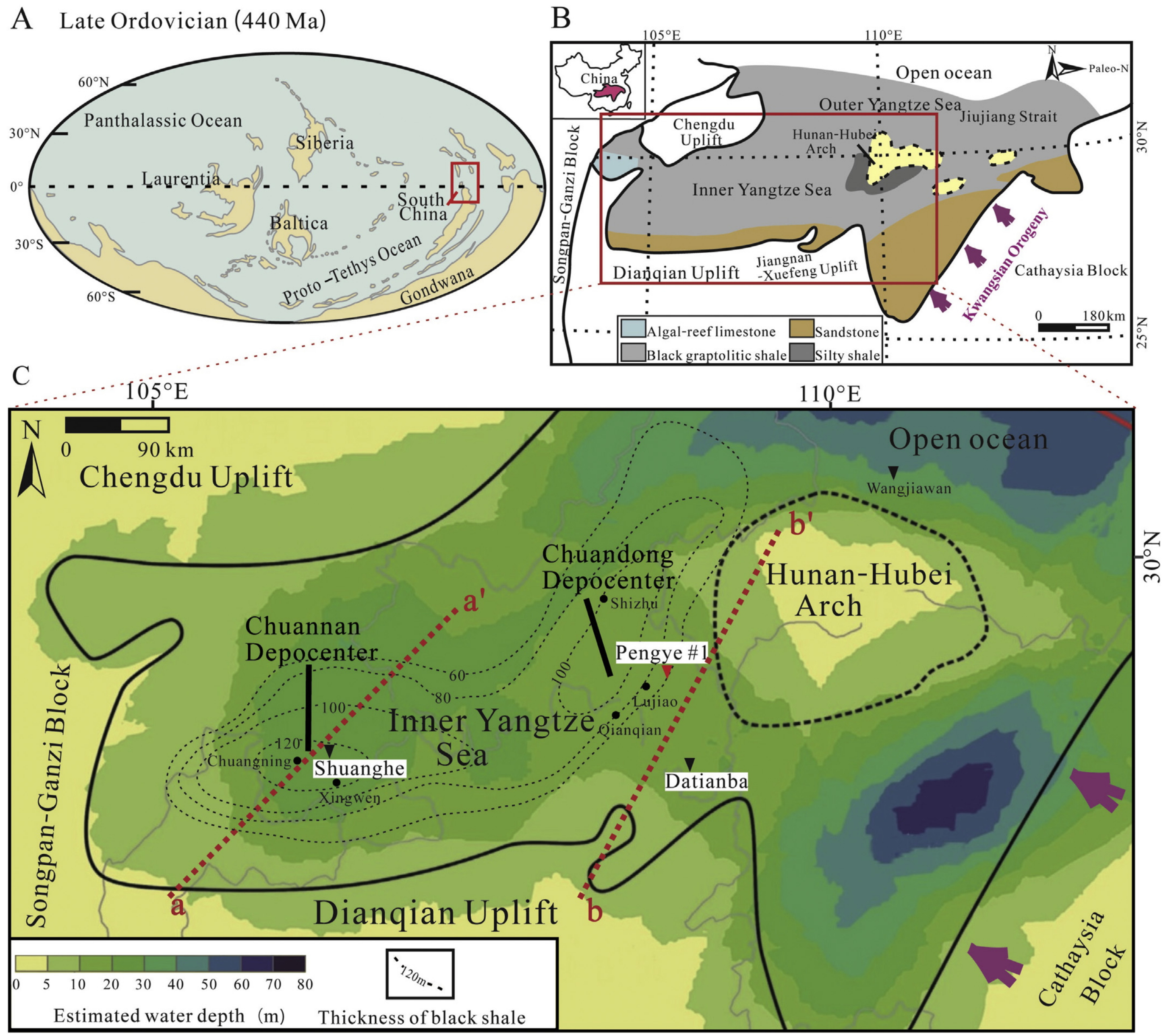

Fig. 1. Geologic setting. (A) Late Ordovician global paleogeography with location of South China (adapted from Ron Blakey, http://jan.ucc.nau.edu/~rcb7/; Zhou et al., 2015). (B) Paleogeography of Yangtze Sea during Ordovician-Silurian transition (after Chen et al., 2004; Yan et al., 2010). (C) Locations of study section (Pengye #1) and three published sections discussed in the text (Shuanghe and Datianba, Liu et al., 2016; Wangjiawan, Fan et al., 2009). This map also shows (i) estimated water depths during mid-Hirnantian glacio-eustatic lowstand (color scale, values in meters; from L. Zhang et al., 2014), and (ii) isopachs for Wufeng and Longmaxi formation black shales, showing locations of the Chuannan and Chuandong depocenters in the inner Yangtze Sea (dotted lines, values in meters; from Liang et al., 2009). Lines a-a′ and b-b′ represent cross-sections in Fig. 8. (For interpretation of the references to color in this figure legend, the reader is referred to the web version of this article.)

than during the glacial peak (Sheehan, 2001; Finnegan et al., 2011), water depths must have been ~100–160 m in the Chuannan depocenter (Shuanghe) and ~80–130 m in the Chuandong depocenter (Datianba) during the pre- and post-Hirnantian intervals. Subaerial exposure of Pengye #1 during the Hirnantian glaciation indicates that water depths at that site were < 70–100 m during the non-glacial intervals.

2.2. Graptolite biostratigraphy and age model

Biostratigraphic studies of the Pengye #1 drillcore have identified the *Dicellograptus complexus* (0–1.45 m), *Paraorthograptus pacificus-Metabolograptus extraordinarius-Metabolograptus persculptus-Akidograptus ascensus* (1.45–5.47 m), and *Parakidograptus acuminatus* zones (5.47–18.20 m), but only the interval from 0 to 8.77 m was analyzed in this study. The boundaries between the *P. pacificus* and *M. extraordinarius* zones and between the *M. persculptus* and *A. ascensus* zones cannot be exactly identified by fossil analyses, but they can be tentatively placed at 3.40 m and 5.0 m based on an organic carbon isotope ($\delta^{13}C_{org}$) profile that shows a prominent positive excursion beginning at ~3.40 m and ending at ~5.0 m, corresponding to these boundaries as observed in other South China sections (Fig. 2; cf. Fan et al., 2009 and Section 5.1). The absence of the Guanyinqiao Bed leads to uncertainty in the position of the *M. extraordinarius* and *M. persculptus* zonal boundary, although it can be tentatively placed at ~4.5 m, which corresponds to the beginning of a decline in $\delta^{13}C_{org}$ as observed in other South China sections (Fig. 2; Fan et al., 2009). Integration of the existing graptolite biostratigraphic and carbon-isotope data suggests the presence of the *D. complexus* (0–1.45 m), *P. pacificus* (1.45–3.4 m), *M.*

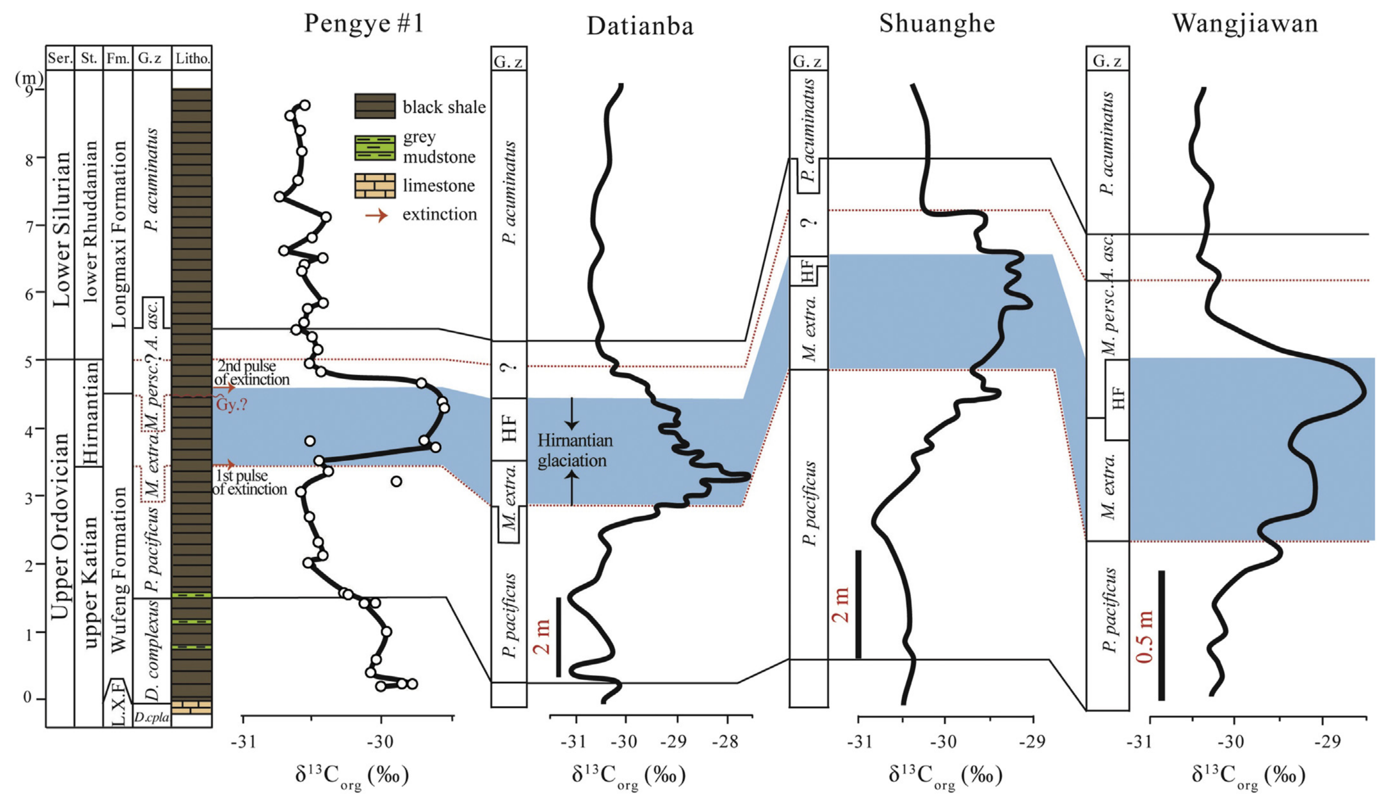

Fig. 2. Biostratigraphic and $\delta^{13}C_{org}$ chemostratigraphic correlations for Pengye #1 (study section), Datianba and Shuanghe (Liu et al., 2016), and Wangjiawan (Fan et al., 2009). Abbreviations: Ser. = Series, St. = Stage, Fm. = Formation, G. z. = Graptolite Zone, Litho. = Lithology, L.X.F. = Linxiang Formation, *D. cpla.* = *D. complanatus*, *M. extra.* = *M. extraordinarius*, *M. persc.* = *M. persculptus*, *A. asc.* = *A. ascensus*, Gy. = Guanyinqiao bed, HF = Hirnantia Fauna. The blue field indicates the peak interval of Hirnantian glaciation. (For interpretation of the references to color in this figure legend, the reader is referred to the web version of this article.)

extraordinarius (3.4–4.50 m), *M. persculptus* (4.5–5 m), *A. ascensus* (5–5.47 m), and *P. acuminatus* zones (5.47–8.77 m). This detailed graptolite zonation of the Pengye #1 core provides a basis for regional and global stratigraphic correlations (Fig. 2; cf. Fan et al., 2013).

Key age tie-points are the Katian-Hirnantian boundary (445.16 Ma) and the Hirnantian-Rhuddanian boundary (443.83 Ma), yielding estimated durations for individual graptolite zones based on international graptolite biozonation schemes for the Ordovician and Silurian (Cooper et al., 2012; Melchin et al., 2012): *D. complexus* ~0.6 Myr, *P. pacificus* ~1.86 Myr, *M. extraordinarius* ~0.73 Myr, *M. persculptus* ~0.60 Myr, *A. ascensus* ~0.43 Myr, and *P. acuminatus* ~0.93 Myr. These data were used to calculate a linear sedimentation rate (LSR) for each graptolite zone (see Section 4.2 and Table 1).

3. Background: redox proxies and controlling factors on $\delta^{34}S$ of pyrite

In order to investigate marine redox conditions in the Pengye #1 core, we used a combination of paleoredox proxies. Fe speciation has been widely used for evaluating local paleoredox conditions (e.g., Li et al., 2010, 2015; Poulton and Canfield, 2011; Jin et al., 2016; J. Shen et al., 2016). Fe associated with carbonate (Fe_{carb}), oxide (Fe_{ox}), magnetite (Fe_{mag}), pyrite (Fe_{py}) are reactive to H_2S during early diagenesis and are collectively termed "highly reactive iron" (Fe_{HR}). The ratio of highly reactive iron to total Fe (Fe_{HR}/Fe_T) is indicative of depositional redox conditions: values < 0.38 and > 0.38 indicate oxic-suboxic and anoxic conditions, respectively (Raiswell and Canfield, 1998; Poulton and Raiswell, 2002; Poulton and Canfield, 2011). In anoxic facies, the presence of H_2S generated by microbial sulfate reduction (MSR) rapidly

Table 1
Thickness and linear sedimentation rates (LSRs) of three study sections by graptolite zones.

Stage	Graptolite zone	Lower boundary age (Ma)	Duration	Pengshui		Datianba		Shuanghe	
				Thickness	LSR	Thickness	LSR	Thickness	LSR
			(Myr)	(m)	(m/Myr)	(m)	(m/Myr)	(m)	(m/Myr)
early Rhuddanian	*C. vesi*	442.47	–	–	–	–	–	–	–
	P. acu.	443.40	0.93	–	0.94[a]	–	1.48[a]	–	1.75[a]
	A. asc.	443.83	0.43	0.97	0.94	1.53	1.48	1.80	1.75
Hirnantian	*M. pers.*	444.43	0.6		0.94		1.48		1.75
	Hirnantia Fauna	–	–	–	–	1.63	3.91	0.18	2.86
	M. extra.	445.16	0.73	1.10	1.51	1.23	3.91	1.91	2.86
late Katian	*P. pacificus*	447.02	1.86	1.95	1.05	4.70	2.57	5.26	2.83
	D. complexus	447.62	0.6	1.45	2.42	1.77	2.95	2.76	4.60

[a] Values were approximately estimated by their neighbors.

converts most Fe_{HR} into pyrite, yielding $Fe_{py}/Fe_{HR} > 0.7–0.8$ (= euxinic conditions), whereas an absence of H_2S results in a smaller fraction of pyrite Fe and $Fe_{py}/Fe_{HR} < 0.7–0.8$ (= ferruginous conditions) (Poulton et al., 2004; Poulton and Canfield, 2011). A minimum Fe_T of 0.5% is required in order to obtain robust Fe speciation results (Clarkson et al., 2014).

The concentrations and ratios of RSTEs (e.g., Mo, U, V) are also useful as paleoredox proxies (Algeo and Maynard, 2004; Tribovillard et al., 2006; Li et al., 2015). Molybdenum (Mo) is present as the soluble, unreactive molybdate anion (MoO_4^{2-}) in oxic facies, whereas in euxinic facies it converts to the particle-reactive thiomolybdate anion ($MoO_{4-x}S_x^{2-}$; x = 1–4) (Erickson and Helz, 2000; Zheng et al., 2000; Helz et al., 2011), which can be taken up by S-bearing organic molecules or Fe-Mo-S minerals and ultimately concentrated in the sediment (Helz et al., 1996; Tribovillard et al., 2004). Therefore, strong Mo enrichments are a salient characteristic of euxinic depositional facies. Based on a compilation of data from modern marine systems, it was shown that Mo enrichments of < 25 ppm are associated with oxic-suboxic bottomwaters, 25–100 ppm with sulfidic porewaters or intermittently euxinic bottomwaters, and > 100 ppm with permanently euxinic bottomwaters (Scott and Lyons, 2012). U enrichment in sediments is limited under oxic-suboxic conditions, when seawater U exists mainly as soluble and unreactive U-carbonate complexes, but it is strongly enriched under anoxic conditions. Its reduction from U(VI) to U(IV) and subsequent uptake by the sediment commences approximately at the Fe (III)-Fe(II) redox boundary rather than under sulfidic conditions (Tribovillard et al., 2006). Several processes accelerate the removal of reduced U from the water column to the sediment, especially adsorption by organic matter and generation of organometallic ligands, so U enrichment commonly correlates with organic carbon abundance (Algeo and Maynard, 2004; McManus et al., 2005). V(V) is reduced to V (IV) under suboxic conditions and to V(III) under euxinic conditions, with an increase in particle reactivity and scavenging rate accompanying each step (Emerson and Huested, 1991; Wanty and Goldhaber, 1992). In addition to local redox conditions and organic substrate availability, the sedimentary accumulation of RSTEs is related to the concentrations of dissolved metals in the water column (Algeo and Lyons, 2006; Algeo and Rowe, 2012; Little et al., 2015).

Another proxy for benthic redox conditions is the molar $C_{org}/P_{reactive}$ ratio, which can be effectively proxied by C_{org}/P_{tot} in organic-rich facies where detrital P and carbonate fluorapatite P is negligible (Algeo and Ingall, 2007; Mort et al., 2010). Oxic conditions enhance the sequestration of remineralized P in sediments through adsorption onto Fe-oxyhydroxides, resulting in sedimentary C_{org}/P_{tot} ratios below the Redfield ratio of 106:1 (Ingall and Jahnke, 1997; März et al., 2008). In contrast, anoxic conditions reductively destroy Fe-oxyhydroxides in the sediment, limiting retention of remineralized P and leading to sedimentary C_{org}/P_{tot} ratios larger than 106:1 as a result of preferential decay of P-bearing compounds and facilitated preservation of organic carbon (Algeo and Ingall, 2007).

The $\delta^{34}S$ value of sedimentary pyrite (i.e., $\delta^{34}S_{py}$) can provide information on seawater sulfate availability during MSR if they formed within the water column (i.e., syngenetic pyrites; e.g., Canfield et al., 2010; Jones and Fike, 2013). The $\delta^{34}S_{py}$ originates from parent sulfate ($\delta^{34}S_{SO4}$) which is altered subsequently by the isotopic fractionation during MSR ($\varepsilon_{MSR} = \delta^{34}S_{SO4} - \delta^{34}S_{py}$). Therefore, $\delta^{34}S_{py}$ is determined mainly by $\delta^{34}S_{SO4}$ and ε_{MSR}. Because both sulfate and organic matter are limiting reactants during MSR, the availabilities of sulfate and organic matter are the first-order controls on ε_{MSR} although many other factors can influence ε_{MSR} in natural systems (e.g., Goldhaber and Kaplan, 1975; Habicht et al., 2002; Jones and Fike, 2013; Leavitt et al., 2013; Algeo et al., 2015; Gomes and Hurtgen, 2015). Given ample sulfate supply, increasing organic availability can increase MSR rate, nonlinearly lowering ε_{MSR} to a minimum value (e.g., 10.9‰ according to Leavitt et al., 2013). Given ample organic supply, small to zero fractionations occur if sulfate concentrations are < 5 mM (Algeo et al., 2015; Gomes and Hurtgen, 2015).

4. Materials and methods

4.1. Samples, geochemical and pyrite-framboid analyses and enrichment factor calculation

Forty-one fresh samples were collected from the Pengye #1 drillcore spanning the entire Wufeng Formation and the lower part of the Longmaxi Formation. Each sample was trimmed to remove surfaces and visible diagenetic features (e.g., pyrite nodules) and then crushed to finer than 200-mesh powder for geochemical analyses. All analyses were carried out in the State Key Laboratory of Biogeology and Environmental Geology, China University of Geosciences (Wuhan).

Total organic carbon (TOC) values were determined by acidification of a sample aliquot to remove carbonate, filtering and washing in distilled water, and analysis using a Jena Eltra 4000 carbon-sulfur analyzer. Accuracy of results was monitored via repeated analysis of Alpha Resources standard AR 4007 (total C = 7.27%) with an analytical error of < 0.2%. Major element concentrations (Fe_T, Al, and Si, etc.) were measured using a Panalytical Epsilon 3^{XLE} X-ray fluorescence spectrometer after powdered samples were fused to glass disks. Analytical errors were under 0.2%.

Fe_{py} was extracted by using the chromium reduction method (Canfield et al., 1986). A powdered sample aliquot was placed in a sealed vessel to react with an acidified $CrCl_2$ solution. The pyrite sulfur was reacted to H_2S and subsequently trapped by silver-nitrate solution through precipitation as Ag_2S. The pyrite Fe concentration was then gravimetrically calculated. The whole experiment was conducted under a purified nitrogen atmosphere to prevent re-oxidation of reduced sulfur. Fe_{carb}, Fe_{ox} and Fe_{mag} were determined using the sequential extraction procedure of Poulton and Canfield (2005). About 100 mg of sample powder was extracted sequentially with solutions of sodium acetate, sodium dithionite, and an oxalic acid-sodium oxalate mixture. All concentrations of extracted iron speciation were diluted 100-fold with 2% HNO_3 and analyzed using atomic absorption spectrometry (AAS), yielding an RSD of < 4%. Unreactive iron (Fe_U), which is mainly in clay minerals and other silicates and is not reactive to H_2S during early diagenesis, was calculated by subtracting Fe_{HR} from Fe_T.

Pyrite sulfur extracted via the chromium reduction method was precipitated as Ag_2S in preparation for measurement of its S-isotopic composition ($\delta^{34}S_{py}$). Isotope measurements were made using a Thermo Fisher Scientific Delta V Plus isotope ratio mass spectrometer coupled with a Flash elemental analyzer. Analytical errors were < 0.2‰ as determined by repeated analyses of standards IAEA S1 ($\delta^{34}S = -0.3$‰), IAEA S2 ($\delta^{34}S = +22.65$‰), and IAEA S3 ($\delta^{34}S = -32.5$‰). The carbon isotopic compositions of organic carbon ($\delta^{13}C_{org}$) were determined by the acidified and rinsed samples using a Finnigan MAT-253 mass spectrometer with analytical errors < 0.1‰.

For trace-element concentrations (including Mo, U, and V), an aliquot of powdered sample was ashed at 600 °C for 12 h in a muffle furnace before dissolution in a Teflon bomb using a standard HF-HCl-HNO_3 digestion protocol. The solution was subsequently analyzed with an Agilent 7700x inductively coupled plasma mass spectrometer (ICP-MS). The analytical precision was better than ± 5% (1σ). Trace-metal enrichment factors (EF) were calculated as:

$$X_{EF} = (X/Al)_{sample}/(X/Al)_{UCC} \quad (1)$$

where the average concentrations of Al and element X in upper continental crust (UCC) were taken from Rudnick and Gao (2003) (1.1 ppm for Mo, 2.7 ppm for U, 97 ppm for V and 8.15% for Al).

Pyrite framboids were measured using a scanning electron microscope (HITACHI-SU8010) in backscattered electron mode. For each sample, > 100 pyrite framboids were selected to measure diameters.

4.2. Calculation of marine productivity fluxes

Marine primary productivity was evaluated using the mass accumulation rates of organic carbon (OCAR) and biogenic silica (SiAR). These fluxes were calculated as:

$$OCAR = TOC \times LSR \times \rho \quad (2)$$

$$SiAR = SiO_{2\,(exc)} \times LSR \times \rho \quad (3)$$

where $SiO_{2(exc)}$ is excess (i.e., non-clay) silica, LSR is linear sedimentation rate (Table 1; calculated as the ratio of thickness to duration for each stratigraphic subdivision, e.g., graptolite zones, in units of m Myr^{-1}), and ρ is bulk rock density (using an assumed mean value of 2.5 g cm^{-3} for black shales, e.g., Shen et al., 2015; Schoepfer et al., 2015). Owing to uncertainties in placement of some graptolite zonal boundaries (see Section 2.2), we adjusted the thicknesses of biozones (within permissible limits of existing biostratigraphic control) to minimize zone-to-zone variations in LSR.

Use of excess silica ($SiO_{2(exc)}$) as a proxy for biogenic silica requires demonstration that the non-clay silica fraction in a sample is of probable biogenic origin, rather than being detrital quartz. Although detrital quartz can potentially covary negatively with clay content, these sediment fractions are more likely to have been co-deposited, so the strong negative correlation between SiO_2 and Al_2O_3 ($r = -0.89$; $p < 0.001$; $n = 36$) at Pengye #1 (Fig. 3B; Table S1) is consistent with non-detrital forms of silica being dominant in the study samples. Examination of the silica fraction of the study samples by scanning electron microscopy (SEM) revealed that silicon is present mostly in amorphous, weakly internally zoned masses (Fig. 4A), which represent an authigenic precipitate (e.g., chert) rather than granular detrital material. The observed features are consistent with a biogenic origin, e.g., as sponge or radiolarian silica that underwent dissolution and secondary reprecipitation (cf. Calvert, 1974; Michalopoulos and Aller, 2004). Furthermore, a recent petrographic study of the Wufeng-Longmaxi shales documented the presence of both sponge and radiolarian fossils (Khan et al., 2019). Therefore, the use of excess silica ($SiO_{2\,(exc)}$) as a proxy for biogenic silica is justified in the present study, which we calculated as:

$$SiO_{2\,(exc)} = [SiO_2]_{sample} - [Al_2O_3]_{sample} \times (SiO_2/Al_2O_3)_{detr} \quad (4)$$

where $(SiO_2/Al_2O_3)_{detr} = 50/23.5$ is based on major-element relationships. Specifically, CaO contents show a moderate negative correlation to Al_2O_3 with an x-axis intercept of ~23.5% (Fig. 3A), which represents the Al_2O_3 content of the pure shale fraction of the study units. Based on this value, a SiO_2-vs-Al_2O_3 crossplot then yields an estimated SiO_2 content for the pure shale fraction of ~50% (Fig. 3B).

5. Results

Key geochemical data for reconstructions of marine redox conditions and marine productivity fluxes in the three study sections and pyrite-framboidal data are shown in Figs. 4–6 and summarized in Tables S1–S3.

5.1. Redox data

Redox data at Datingba and Shuanghe sections can be found in Liu et al. (2016) and the results for the Pengye #1 drillcore are described here. C_{org}/P_{tot} ratios are 56–252 (mean 140) in the lower *D. complexus* Zone and increase with large fluctuations to 118–1357 (mean 458) in the upper *D. complexus* to *M. extraordinarius* zones, before declining to 135–296 (mean 193) in the *M. persculptus* to *P. acuminatus* zones.

All samples yield Fe_T values > 1% which are higher than the threshold value of 0.5% for robust iron speciation results (Clarkson et al., 2014). The Fe_U in detrital silicates was the highest at Pengye #1 (mean 1.1%) and lowest at Shuanghe (mean 0.2%) with the Datianba in the middle (mean 0.7%), consistent with the relative water depths inferred for the study sections (i.e., Shuanghe > Datianba > Pengye #1; see Section 2). Fe_{HR}/Fe_T and Fe_{py}/Fe_{HR} ratios show similar stratigraphic patterns, with increases upsection within the Wufeng Formation and relatively stable values in the Longmaxi Formation (Fig. 5). Fe_{HR}/Fe_T ratios are 0.19–0.46 (mean 0.28) in the *D. complexus* Zone, 0.38–0.96 (mean 0.60) in the *P. pacificus* and *M. extraordinarius* zones, and 0.42–0.83 (mean 0.63) in the upper three zones. Fe_{py}/Fe_{HR} ratios are 0.30–0.72 (mean 0.54) in the *D. complexus* Zone, 0.36–0.93 (mean 0.74; except for one low value of 0.29) in the *P. pacificus* to *M. extraordinarius* zones, and 0.64–0.85 (mean 0.72) in the upper three zones.

RSTE profiles exhibit broadly similar trends (Fig. 5). The *D. complexus* Zone exhibits generally low values: Mo = 2.0–15.7 ppm (mean 5.2 ppm), U = 5.5–10.6 ppm (mean 7.3 ppm), and V = 144–419 ppm (mean 217 ppm). The *P. pacificus* to *A. ascensus* zones have a wider range of RSTE concentrations: Mo = 9–123 ppm (mean 58 ppm), U = 8–108 ppm (mean 30 ppm), and V = 156–1077 ppm (mean 717 ppm). The *P. acuminatus* Zone yields relatively high RSTE concentrations: Mo = 36–80 ppm (mean 65 ppm), U = 13–33 ppm (mean

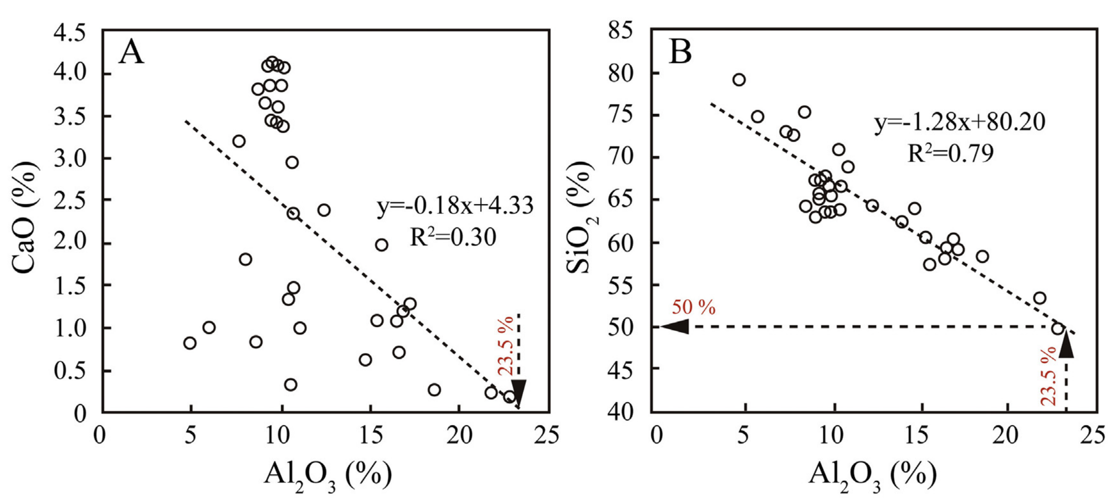

Fig. 3. Crossplots of CaO vs Al_2O_3 (A), and SiO_2 vs Al_2O_3 (B) for Pengye #1 section. These crossplots permit estimations of the Al_2O_3 and SiO_2 contents of the pure shale endmember in the study section, which consists mainly of siliceous shales. The dashed line in A represents the regression used to estimate a ~23.5% Al_2O_3 content for pure (non-siliceous) shale, and the dashed line in B represents a regression showing that this Al_2O_3 value is associated with a SiO_2 content of ~50% (see the dashed arrow lines). Higher silica contents are due to the presence of biosilica (of sponge or radiolarian origin; Khan et al., 2019), which generates a negative relationship because of dilution effects in a two-component mixing system (i.e., clays and biosilica).

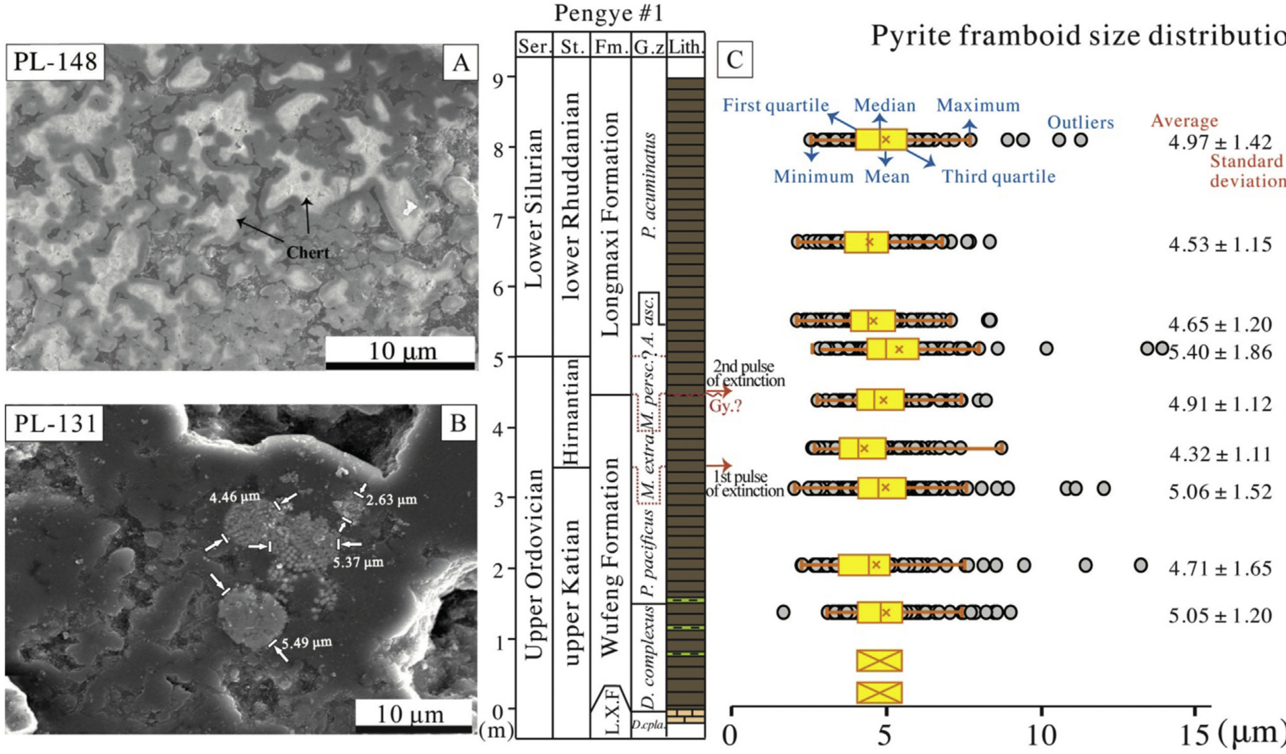

Fig. 4. Petrological characteristics of the Pengye #1 section. (A) Scanning electron microscope (SEM) image of amorphous silica (chert) in a typical sample PL-148 from 1.42 m in Pengye #1 section. Examination of SEM images (n = 17) revealed little detrital quartz; most silica is of the amorphous variety shown here, which is of biogenic origin. (B) SEM image of framboidal pyrites in sample PL-131 from 3.52 m in Pengye #1 section. (C) Pyrite-framboidal size distribution and 'box-and-whisker' plots for Pengye #1 section. Lithological legend and abbreviations as in Fig. 2.

21 ppm), and V = 376–752 ppm (mean 565 ppm).

$\delta^{34}S_{py}$ values in the *D. complexus* and *P. pacificus* zones fluctuated between −26‰ and −12‰ (Fig. 6). The $\delta^{34}S_{py}$ profile exhibits a ca. +20‰ excursion from the *M. extraordinarius* to the lower *M. persculptus* zones, stabilizing around −10‰ to −5‰ in the upper *M. persculptus* to *P. acuminatus* zones. $\delta^{13}C_{org}$ values decline gradually from −29.8‰ to −30.6‰ upsection through the *D. complexus* and *P. pacificus* zones, then exhibit a sharp positive excursion to −29.6‰ within the *M. extraordinarius-M. persculptus* zones (i.e., Hirnantian glacial interval), before shifting negatively and stabilizing around −30.6‰ in the *A. ascensus* to *P. acuminatus* zones (Fig. 2).

5.2. Productivity data

At Pengye #1, TOC contents are 1.3–3.8% (mean 2.9%) in the *D. complexus* Zone, 2.0–8.7% (mean 4.4%) in the *P. pacificus* Zone, and 2.7–4.6% (mean 3.7%) in the *M. extraordinarius* to *P. acuminatus* zones. We further calculated OCAR values for all study sections in order to infer spatiotemporal variation of primary productivity (Fig. 6). At Pengye #1, OCAR (in units of mg cm^{-2} kyr^{-1}) shows fluctuating values from 5.2 to 22.9 (mean 13.2) in the *D. complexus* to *M. extraordinarius* zones, and then remain relatively stable (7.4–10.9; mean 8.5) in the *M. persculptus-P. acuminatus* zones (Fig. 6). At Datianba, OCAR values are 15.9–37.9 (average 22.9) in the *D. complexus* to *P. pacificus* zones, and then increase sharply from the top of the *P. pacificus* Zone with a peak in the *M. extraordinarius* Zone (28.3–81.3, mean 47.0). The Guanyinqiao Bed and *P. acuminatus* Zone show low OCAR values (3.7–23.5, mean 10.1). At Shuanghe, OCAR averages 38.0 in the *D. complexus* Zone, decreases to 22.8 in the lower-mid *P. pacificus* Zone, rises to 31.8 in the upper *P. pacificus-M. extraordinarius* zones, falls to a minimum of 14.2 in the Guanyinqiao Bed, and then recovers to 27.9 in the *M. persculptus-P. acuminatus* zones (Fig. 6).

5.3. Petrographic data

At Pengye #1, although both framboidal and euhedral pyrite crystals were observed, they were too few to be measured for statistics of their size distribution in the samples from the *D. complexus* Zone. For the overlying strata, pyrite crystals are mostly small framboids that occur randomly distributed within samples. These samples yield framboids with a mean diameter ranging from 4.3 to 5.4 μm and a standard deviation of 1.1 to 1.9 μm (Fig. 4B–C).

6. Discussion

6.1. Evaluation of diagenetic effects for used proxies

Thermal maturation results in substantial loss of organic carbon as hydrocarbons are generated (Raiswell and Berner, 1987), and elemental redistribution or loss can occur in shales as a result (see Section 2.1; cf. Abanda and Hannigan, 2006; Ross and Bustin, 2009). All three sections we studied experienced thermal histories with maximum burial temperatures of ~210–250 °C according to backstripping analyses, measurement of vitrinite reflectance (~2.0%), and analysis of clay minerals (cf. Qing et al., 2009; Li et al., 2012; Nie et al., 2012; J.K. Zhang et al., 2014). However, thermal maturation is unlikely to alter secular trends of TOC in a single section, nor between the three study sections given their similar thermal histories within a single basin (Qing et al., 2009; Nie et al., 2012). Although minor diagenetic changes are possible, trace elements such as Mo, U, V continue to show strong enrichment in most samples of Pengye #1, implying only limited loss due to thermal maturation. Studies of TM (trace metal) -TOC relationships spanning multiple basins of varying thermal characteristics (e.g., Algeo et al., 2007) have documented patterns consistent with primary marine relationships and not found any obvious large-scale thermal effects. This may be due, in part, to the low permeability of fine-grained siliciclastic

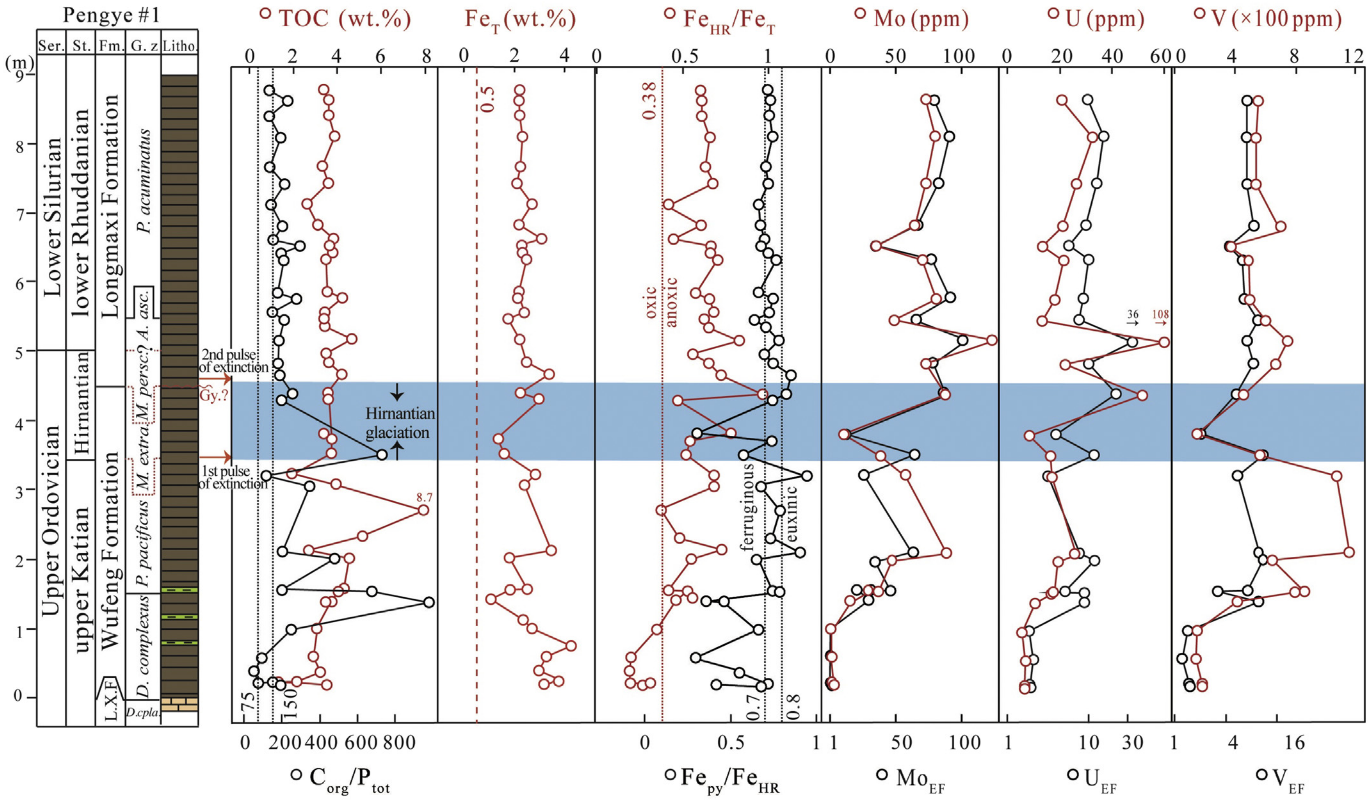

Fig. 5. Chemostratigraphic profiles of TOC, C_{org}/P_{tot}, Fe_T, Fe_{HR}/Fe_T, Fe_{py}/Fe_{HR}, Mo-U-V concentrations, Mo_{EF}, U_{EF}, and V_{EF} for Pengye #1. The C_{org}/P_{tot} values of 75 and 150 represent oxic-suboxic and suboxic-anoxic redox thresholds, respectively (Algeo and Ingall, 2007). The values of 0.38 (for Fe_{HR}/Fe_T) and 0.7–0.8 (for Fe_{py}/Fe_{HR}) are used to distinguish oxic-suboxic from anoxic conditions and anoxic-ferruginous from anoxic-euxinic conditions, respectively (Raiswell and Canfield, 1998; Poulton and Raiswell, 2002). Fe speciation analysis was limited to siliciclastic samples with $Fe_T > 0.5\%$ (cf. Clarkson et al., 2014). Lithological legend and abbreviations as in Fig. 2.

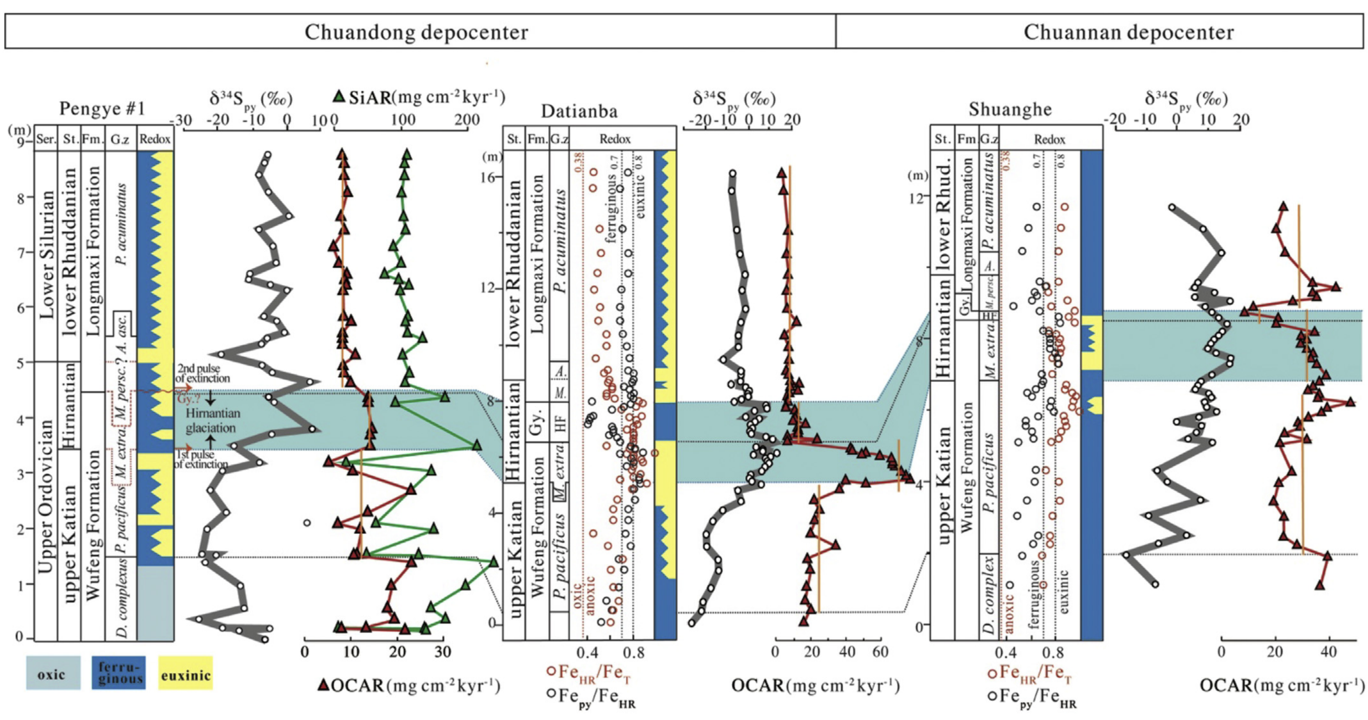

Fig. 6. Comparison of redox conditions, pyrite sulfur isotopic compositions ($\delta^{34}S_{py}$), and productivity indicators for three OST sections. The Fe-speciation data for the Datianba and Shuanghe sections and S-isotope data are from Liu et al. (2016), and OCAR (mass accumulation rates of organic carbon) values are calculated from TOC contents given in Liu et al. (2016) (Table S3). Abbreviations as in Fig. 2.

sediments, which limits migration and loss of trace elements released from decaying organic matter (Abanda and Hannigan, 2006). Thermal maturation also probably had some effects on Fe speciation, with alteration converting some oxide iron into silicate minerals (Raiswell et al., 2008). However, pronounced coupling between redox-sensitive trace-element and Fe-speciation data (see Section 6.2) imply that effects on Fe speciation were minimal. Pyrite sulfur remains largely intact during burial even to low-grade metamorphic conditions (Raiswell and Berner, 1987), resulting in little influence on $\delta^{34}S_{py}$ signals. Taken together, the geochemical indices that we measured are inferred not to have been significantly modified by diagenesis and, therefore, to provide a robust record of primary environmental conditions and processes.

6.2. Reconstruction of redox conditions at Pengye #1 during the OST

At Pengye #1, the lower part of the *D. complexus* Zone (0–1.40 m) was characterized by slightly variable, oxic to suboxic conditions. Low Fe_{HR}/Fe_T ratios (< 0.38) are consistent with oxic conditions (Poulton and Raiswell, 2002), and intermediate C_{org}/P_{tot} ratios (82–252; mean 140) with mainly suboxic conditions. RSTEs yield EFs close to or slightly higher than upper continental crustal (UCC) values: Mo_{EF} of 1.3–3.3, U_{EF} of 1.7–2.5, and V_{EF} of 1.3–1.8, which are consistent with redox conditions in the oxic to suboxic range (Tribovillard et al., 2006).

The upper *D. complexus* to *P. acuminatus* zones were deposited under dominantly anoxic conditions, as indicated by Fe_{HR}/Fe_T ratios that are mostly > 0.38 and elevated C_{org}/P_{tot} ratios (118–678; mean 246). These conditions fluctuated between ferruginous and euxinic, as indicated by variable Fe_{py}/Fe_{HR} ratios (from 0.29 to 0.93, with a mean of 0.71). These redox inferences are confirmed by trace-metal data: U, V, and Mo are significantly enriched relative to UCC, with Mo_{EF} of 11.9–170.2, U_{EF} of 4.7–61.0, and V_{EF} of 2.5–15.2. Mo concentrations mostly vary between 25 and 100 ppm, which is also indicative of intermittently euxinic conditions (Scott and Lyons, 2012). Mo and V concentrations exhibit good positive relationships with Fe_{py}/Fe_{HR} ($r = +0.61$; $p < 0.01$ and $+0.67$; $p < 0.001$, respectively; $n = 23$; not shown), but U exhibits only a weak and statistically non-significant positive correlation with this proxy ($r = +0.36$, $p > 0.05$; $n = 23$; not shown). Higher Mo and V concentrations are found in euxinic samples relative to ferruginous samples, indicating the importance of H_2S for uptake of these RSTEs, whereas U concentrations are nearly the same in euxinic and ferruginous samples, indicating a lack of influence by H_2S (Algeo and Maynard, 2004).

In summary, the Pengye #1 section accumulated under oxic conditions during much of the period of *D. complexus* Zone but shifted to anoxia from the late Katian (*P. pacificus* Zone) to the early Rhuddanian, with fluctuations between euxinic and ferruginous conditions (Fig. 6).

6.3. Redox heterogeneity in inner Yangtze Sea during the OST

In order to evaluate spatiotemporal variation of marine redox conditions in the inner Yangtze Sea during the OST, our results for Pengye #1 were compared with redox proxy data for two other sections located in the same basin, Datianba and Shuanghe (Fig. 6; Liu et al., 2016). The depositional redox conditions of these two sections were evaluated using the same combination of Fe speciation and trace-metal enrichment data as for Pengye #1. Datianba and Shuanghe were deposited under anoxic ferruginous conditions during the period of *D. complexus* Zone, contrasting with the coeval oxic conditions that prevailed at Pengye #1. This redox discrepancy further supports the shallowest water depth for the Pengye #1 among study section (see Section 2) and also consistent with the highest Fe_U at the Pengye #1 (mean 2.4% at Pengye #1 versus 0.4–0.6% at Datianba and Shuanghe; Tables S2–S3). Subsequently, from the latest Katian to early Rhuddanian, persistent-to-intermittent euxinia was dominant at Datianba except for a ferruginous interval during the late stage of Hirnantian glaciation (i.e., Guanyinqiao Bed), whereas Shuanghe was mainly characterized by ferruginous conditions but shifted to euxinic conditions during the *M. extraordinarius* Zone.

A close comparison of redox states among these three sections further demonstrates a heterogeneous redox evolution in the inner Yangtze Sea during the OST. During the early late Katian (*D. complexus* Zone; Fig. 6), the inner Yangtze Sea was mainly characterized by ferruginous anoxic conditions with local oxic-suboxic bottom-water conditions. During the late Katian (*P. pacificus* Zone; Fig. 6), H_2S gradually began to expand in the Chuandong depocenter while ferruginous waters still occupied the Chuannan depocenter. During the early Hirnantian (*M. extraordinarius* Zone), both depocenters were characterized by euxinic conditions. With the glacio-eustatic fall of the early to middle Hirnantian, many marine sections shifted toward more oxygenated conditions (cf. Brenchley et al., 1995; Chen et al., 2004; Yan et al., 2012). However, the early Hirnantian in the Datianba and Shuanghe sections was characterized by enhanced euxinia, which runs counter to interpretations by Yan et al. (2012) but corresponds to redox inferences from pyrite-S isotope data by Zhang et al. (2009) and Hammarlund et al. (2012). During the middle Hirnantian (Guanyinqiao Bed; Fig. 6), euxinia seemingly disappeared in the inner Yangtze Sea, which experienced a modest shift toward better oxygenated conditions (cf. Zhou et al., 2015; Chen et al., 2016). From the late Hirnantian to early Rhuddanian (Fig. 6), reducing conditions were re-established in the inner Yangtze Sea, with re-appearance of euxinia in the Chuandong depocenter.

6.4. Watermass restriction of inner Yangtze Sea during the OST

The inner Yangtze Sea was a semi-isolated basin during the OST (Chen et al., 2004), although the degree of watermass restriction may have varied owing to its complex bathymetry. Mo/TOC ratios can be used to provide insights regarding hydrographic restriction under reducing conditions (Algeo and Lyons, 2006). For the Upper Ordovician Wufeng Formation, black shales in the Chuannan depocenter yield Mo/TOC ratios (mean 3.8 ppm/wt%; red line in Fig. 7) indicative of severe watermass restriction (similar to the modern Black Sea, 4.5 ppm/wt%), whereas those in the Chuandong depocenter yield a wider range of moderately higher ratios (mean 15.7 ppm/wt%; yellow line in Fig. 7),

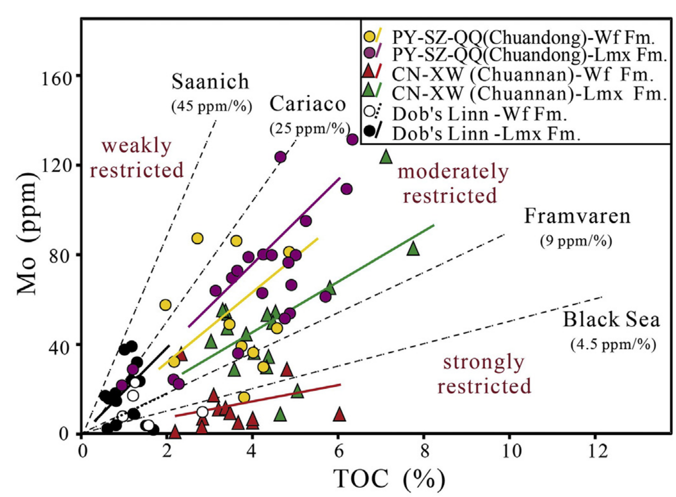

Fig. 7. Crossplot of Mo versus TOC for three OST sections. Dashed lines reflect degrees of restriction based on modern marine systems (Algeo and Lyons, 2006). Abbreviations: PY = Pengye #1, SZ = Shizhu, QQ = Qianqian, CN = Changning, and XW = Xingwen sections; Wf = Wufeng, Lmx = Longmaxi. Data for Shizhu, Qianqian, Changning and Xingwen sections are from Li et al. (2017a). Data for Dob's Linn in Scotland, the GSSP of the Ordovician-Silurian boundary, are shown as representative of a coeval open-marine system (after Hammarlund et al., 2012).

reflecting an intermediate degree of restriction. For the lower Silurian Longmaxi Formation, black shales in the Chuannan depocenter yield Mo/TOC ratios (mean 11.3 ppm/wt%; green line in Fig. 7) indicative of moderately severe restriction (similar to the modern Framvaren Fjord, 9 ppm/wt%), whereas those in the Chuandong depocenter yield ratios (mean 18.9 ppm/wt%; purple line in Fig. 7) indicative of moderately open conditions (similar to the modern Cariaco Basin, 25 ppm/wt%). The spatial differences in Mo/TOC ratios show that Chuandong depocenter was less restricted than the Chuannan depocenter, probably because its location was in the outer part of the inner Yangtze Sea and, thus, closer to the open ocean.

Because there is some uncertainty whether the trace-metal inventories of OST seawater were similar to those of modern seawater, a comparison of the Mo/TOC ratios of the present study units with those at Dob's Linn, Scotland, is warranted (Fig. 7). Dob's Linn, the GSSP for the Ordovician-Silurian system boundary, accumulated on a continental slope of the Iapetus Ocean (Cocks and Torsvik, 2002) and, thus, almost certainly under unrestricted marine conditions. Dob's Linn exhibits considerable scatter in Mo/TOC ratios, in part because of its generally low Mo and TOC concentrations, but a cluster of samples with ratios at 25–45 is similar to those values of < 550 Ma (average 27; Scott et al., 2008), consistent with near-modern Mo concentrations in Ordovician seawater. For this reason, we infer that the modern reference basins (i.e., Black Sea, Framvaren Fjord, and Cariaco Basin) provide a reasonable benchmark for interpreting watermass restriction in the study units. In summary, the Chuannan and Chuandong depocenters in the inner Yangtze Sea experienced substantial but variable watermass restriction during the OST.

Restriction of the inner Yangtze Sea may have been due to a combination of tectonic (Kwangsian Orogeny) and eustatic factors (Hirnantian glaciation). The Kwangsian Orogeny was a compressional event related to stepwise convergence of the Yangtze and Cathaysia blocks during the Late Ordovician to Early Silurian (Chen et al., 2014). It was initiated in the area of modern southeastern coastal China and progressed in a northwestward direction, generating the semi-isolated Yangtze Basin along the compressional margin. In addition, glacial eustatic changes may have resulted in large water-depth changes over the relatively short (~1-million-year) Hirnantian glacial interval (Rong et al., 2011; Liu et al., 2016; Liu et al., 2017). All of these may have reinforced the restriction of the inner Yangtze Sea observed here.

6.5. Marine productivity in inner Yangtze Sea during the OST

TOC concentrations in rocks are affected by the quantity and type of sinking organic matter through carbon fixation processes in the surface ocean, organic preservation conditions, and sedimentation rates (Canfield, 1994; Schoepfer et al., 2015). Most organic matter decomposes within the oxic water column or at the sediment-water interface or is lost during geological burial, and the preserved TOC content of sedimentary rocks usually represents only a small fraction of original primary productivity. The study sections exhibit similar ranges (ca. -27 to -31‰) and stratigraphic patterns of $\delta^{13}C_{org}$ variation (Fig. 2), implying similar assemblages of primary producers (Zhang et al., 2013; B. Shen et al., 2016). Given equivalence among the three study sections with regard to primary producers, redox conditions (see Sections 6.2 and 6.3), and burial histories (see Section 2.1), it should be possible to evaluate relative variations in primary productivity rates on the basis of organic carbon accumulation rate (OCAR), which removes the effect of varying sedimentation rates on TOC content. Biogenic silica fluxes from siliceous plankton such as diatoms and radiolarians can also reflect marine primary productivity (Ragueneau et al., 2000; de Wever et al., 2001). At Pengye #1, the accumulation rates of biogenic silica (SiAR) and OCAR show a significant correlation ($r = +0.72$, $p < 0.01$, $n = 36$; not shown). Since all accumulation rates depend on sedimentation rates, such covariation might be forced by the LSR term in both equations, but this possibility is largely disproven by a similar correlation between $SiO_{2\ (exc)}$ and TOC concentrations ($r = +0.60$, $p < 0.01$, $n = 36$; not shown). Thus, we infer that OCAR is an effective proxy for evaluation of relative primary productivity rates in the inner Yangtze Sea.

A comparison of primary productivity levels among the three study sections shows large differences across the Yangtze Basin (Fig. 6). At Pengye #1, OCAR values are low to moderate (5.2–22.9, mean 11.3; note: all fluxes are in units of mg cm^{-2} kyr^{-1}) with significant fluctuations during deposition of the Wufeng Formation. At Datianba, OCAR values range from 3.7 to 37.9 (mean 13.2) in the *D. complexus*-middle *P. pacificus* zones and Guanyinqiao Bed−*P. acuminatus* Zone, followed by higher values (28.3–81.3, mean 40.7) in the upper *P. pacificus* to *M. extraordinarius* zones. At Shuanghe, OCAR values range from 8.3 to 42.6 (mean 25.5) in the *D. complexus*-middle *P. pacificus* zones and Guanyinqiao Bed−*P. acuminatus* Zone but increase in the upper *P. pacificus-M. extraordinarius* zones (19.3–45.0; mean 31.8). To generalize, primary productivity during the OST was low to moderate at Pengye #1 and higher at Datianba and Shuanghe, and these differences were most pronounced in the *M. extraordinarius* Zone. OCAR values at study all sections fell during the interval of deposition of the Guanyinqiao Bed, corresponding to the disappearance of black shales and to full development of Hirnantian glaciation.

6.6. Mechanisms controlling marine euxinia in inner Yangtze Sea during the OST

Our integrated redox dataset demonstrates pronounced spatiotemporal heterogeneity of redox conditions—especially the development of euxinic conditions in the inner Yangtze Sea during the OST (see Sections 6.2 and 6.3). Liu et al. (2016) proposed that this redox heterogeneity was linked to Hirnantian glacio-eustasy and tectonic movements of the regional Kwangsian Orogeny, although watermass restriction served as a first-order control on water-column anoxia. Here, we explore further the controlling mechanisms on development of marine euxinia in the inner Yangtze Sea during the OST.

Under euxinic conditions, dissolved sulfate is the main oxidant used in microbial breakdown of organic matter. The generated H_2S is converted to pyrite through reaction with reactive Fe (Fe_{HR}) in a 2:1 molar ratio. If Fe_{HR} supply is inadequate, H_2S will accumulate in the water column, and euxinic conditions develop. Therefore, the development of euxinia depends on the relative fluxes of Fe_{HR} and H_2S in the marine system, with production of the latter controlled by marine sulfate availability and primary productivity levels (Raiswell and Canfield, 2012; Feng et al., 2014).

6.6.1. Pre-glacial and post-glacial intervals

During the latest Katian (pre-glacial interval) and the latest Hirnantian-early Rhuddanian (post-glacial interval), euxinic conditions existed at Pengye #1 and Datianba in the Chuandong depocenter, but persistently ferruginous conditions existed at Shuanghe in the Chuannan depocenter (Fig. 6). The development of ferruginous conditions requires that the H_2S flux generated by MSR was insufficient to react fully with available Fe_{HR} (cf. Feng et al., 2014). The ferruginous samples in the Chuannan depocenter (Shuanghe) are characterized by low Fe_U (< 0.4%; Table S3), which represents Fe in clay minerals and other silicates from terrestrial sources, indicating a limited detrital Fe flux. In contrast, the euxinic samples in the Chuandong depocenter exhibit higher Fe_U concentrations (mean 1.3% at Pengye #1 and 0.7% at Datianba; Tables S2 and S3), indicating greater detrital Fe fluxes. Differences in Fe_U are mirrored by differences in Fe_T, with lower Fe_T values at Shuanghe (1.1–1.8%, mean 1.2%; Liu et al., 2016; Table S3) versus higher Fe_T values at Datianba (1.7–3.4%, mean 2.5%; Liu et al., 2016; Table S3) and Pengye #1 (1.8–3.5%, mean 2.5%; Table S2), providing further evidence of low Fe availability in the Chuannan depocenter.

Limited quantities of organic matter to drive MSR have been proposed to explain the absence of euxinia in some Precambrian marine systems (e.g., Johnston et al., 2010; Poulton et al., 2010). However, differences in productivity levels among the present study sections (see Section 6.5) are inconsistent with an organic matter control on development of euxinia. In the *P. pacificus* Zone, productivity levels at Shuanghe (OCAR mean 28.4 mg cm^{-2} myr^{-1}) are similar to or higher than levels at Datianba (OCAR mean 29.8) and Pengye #1 (OCAR mean 12.9) (Fig. 6). Furthermore, in the *M. persculptus-P. acuminatus* zones, productivity levels at Shuanghe (OCAR mean 27.9) are also higher than at Datianba (OCAR mean 11.4) and Pengye #1 (OCAR mean 8.5) (Fig. 6). Therefore, regional differences in primary productivity levels cannot account for ferruginous conditions at Shuanghe versus euxinic conditions at Datianba and Pengye #1.

The existence of ferruginous conditions in the Chuannan depocenter despite limited Fe availability and high organic carbon fluxes must therefore have been due to low sulfate availability during the OST. Since sulfate availability was sufficient for development of euxinia in the Chuandong depocenter at that time, these considerations suggest strong spatial variation in seawater sulfate availability across the inner Yangtze Sea. Global seawater sulfate concentrations are considered to have been relatively low but variable during the Cambrian and Ordovician periods (< 2–12 mM; Gill et al., 2007; Halevy et al., 2012; Thompson and Kah, 2012; Algeo et al., 2015), consistent with evidence of strong local variability in aqueous sulfate concentrations in North American basins (Kah et al., 2016; Young et al., 2016). Low sulfate availability in the inner Yangtze Sea during the OST may have been due in part to hydrological restriction (see Section 6.4), with spatial variations in the degree of restriction and primary productivity levels contributing to local variability in sulfate concentrations under such conditions. At low sulfate concentrations, spatial variations in point source fluxes may have also contributed to local variability, leading to locally higher sulfate concentrations around river mouths (i.e., riverine sulfate source) or deep sills connecting the inner Yangtze Sea to the outer Yangtze Sea and global ocean (i.e., seawater sulfate source). During the studied intervals, the Chuandong depocenter was proximal to tectonic uplifts (e.g., Dianqian Uplift) associated with the Kwangsian Orogeny on the southeastern margin of the Yangtze Sea (Chen et al., 2014) and to the open ocean (Fig. 1), potentially resulting in higher sulfate supply from both riverine and seawater sources (Fig. 8A; Liu et al., 2016). Glacio-eustatic fluctuations would have had a particularly pronounced effect on open-ocean resupply of sulfate, as higher sea-level elevations during non-glacial intervals would have led to enhanced watermass exchange across the bounding sills of the inner Yangtze Sea (Fig. 8A). On the other hand, the Chuannan depocenter was located further from both tectonic uplifts and the open ocean, thus limiting sulfate resupply from both riverine and open-ocean sources (Fig. 8A).

The development of spatial variability in seawater sulfate concentrations within the inner Yangtze Sea may be evidenced by the $\delta^{34}S_{py}$ records of the present study sections. Although diagenetic pyrite formed within the sediment is prone to large variations in $\delta^{34}S$ as a result of Rayleigh distillation of porewater sulfate (Lyons et al., 2009), syngenetic pyrite crystals formed in the water column commonly exhibit nearly uniform $\delta^{34}S$ compositions (e.g., Nielsen and Shen, 2004). The syngenetic origin of the pyrite framboids in the present study sections is confirmed by their small size and limited size variation (cf. Wilkin et al., 1996; Wilkin and Barnes, 1997; Wignall and Newton, 1998): the mean framboid diameters are 4.84 ± 1.36 μm at Pengye #1 (Fig. 4C; this study) and 5.19 ± 2.00 μm at Shuanghe (Zou et al., 2017). Therefore, the $\delta^{34}S_{py}$ of the study units can be used to evaluate contemporaneous seawater sulfate concentrations and isotopic compositions (cf. Algeo et al., 2015).

The $\delta^{34}S_{py}$ values differ markedly between the two depocenters of the inner Yangtze Sea. In the *P. pacificus* Zone (pre-glacial interval), the Chuandong depocenter yields substantially lower $\delta^{34}S_{py}$ values (mean −22.1‰ at Pengye #1, −18.4‰ at Datianba) than the Chuannan depocenter (mean + 3.8‰ at Shuanghe). The same pattern is observed in the *M. persculptus-P. acuminatus* zones (post-glacial interval): the Chuandong depocenter yields much lower $\delta^{34}S_{py}$ values (mean −5.2‰ at Pengye #1, −3.7‰ at Datianba) than the Chuannan depocenter (mean + 8.7‰ at Shuanghe). These differences in mean $\delta^{34}S_{py}$ values imply a spatial gradient in either aqueous sulfate concentrations, sulfate $\delta^{34}S$, or both across the inner Yangtze Sea during the OST. If the degree of MSR fractionation was more-or-less uniform across the inner Yangtze Sea, then this variation reflects a gradient in aqueous sulfate $\delta^{34}S$, with higher values (by 10–25‰) in the Chuannan depocenter relative to the Chuandong depocenter. On the other hand, if MSR fractionation varied owing to differential sulfate concentrations, then differences of 10–25‰ in $\delta^{34}S_{py}$ imply fairly large differences in seawater sulfate concentrations between the two depocenters (cf. Algeo et al., 2015). In either case, such differences can be attributed to generally high seawater sulfate concentrations with higher ^{32}S-rich sulfate fluxes from weathering and open-ocean sources into the Chuandong depocenter than those into the Chuannan depocenter given that Chuandong depocenter was closer both to the tectonically active Dianqian Uplift and open ocean (Fig. 1C). We note that similar spatial gradients in $\delta^{34}S_{py}$ have been documented for the Ediacaran Doushantuo and lower Cambrian Niutitang formations in South China, also linked to small marine sulfate reservoir size and locally elevated sulfate weathering fluxes (Li et al., 2010; Feng et al., 2014; Jin et al., 2016).

6.6.2. Hirnantian glacial interval

During the *M. extraordinarius* Zone (i.e., early stage of Hirnantian glaciation), euxinic waters developed at all three study sections, which can be attributed to higher sulfate availability (Fig. 8B). Although declining temperatures may have reduced chemical weathering intensity during the glacial interval (Gibbs and Kump, 1994), the glacio-eustatic fall exposed pyrite-rich shelf sediments to weathering, resulting in a local increase in sulfate weathering flux (Fig. 8B). Such an increase in sulfate supply may have been a key factor causing the watermass of the Chuannan depocenter (Shuanghe) to shift from ferruginous to euxinic conditions. At the maximum glacial lowstand, however, a shift away from euxinic conditions was induced by a combination of: (1) reduced primary productivity (possibly as a result of cooler sea-surface temperatures or more limited nutrient supply), and (2) reduced sulfate supply owing to dwindling erosion of exposed shelves and increasing hydrological restriction from the open ocean as basin-margin sills shallowed or became subaerially exposed (Fig. 8C). This interpretation is supported by a decline in OCAR from the *M. extraordinarius* Zone to the Guanyinqiao Bed, which is particularly pronounced at Datianba and Shuanghe (Fig. 6).

The Hirnantian inner Yangtze Sea was characterized by a large spatial gradient in $\delta^{34}S_{py}$: mean values were −4.1‰ at Pengye 1#, +6.7‰ at Datianba, and +13.2‰ at Shuanghe during the early glacial interval (*M. extraordinarius* Zone), and +4.2‰ at Datianba and +12.6‰ at Shuanghe during deposition of the Guanyinqiao Bed (Fig. 6; Tables S1, S3), which is similar to the gradients observed for the pre- and post-glacial periods (see Section 6.6.1). These gradients can be similarly attributed to larger ^{32}S-rich sulfate fluxes from weathering and open-ocean sources to the Chuandong depocenter (relative to the Chuannan depocenter) owing to its proximity to the tectonically active Dianqian Uplift and the open ocean (cf. Section 6.6.1). These patterns suggest a persistence of similar local controls on sulfate fluxes from the pre-glacial interval through the post-glacial interval.

Although local factors may have influenced sulfate fluxes to the inner Yangtze Sea, secular variation in $\delta^{34}S_{py}$ profiles suggests that the Hirnantian inner Yangtze Sea also responded to global sulfur-cycle changes. This inference is based on a common positive $\delta^{34}S_{py}$ excursion in all three study sections during the Hirnantian glacial interval (Fig. 6), which is also observed in OST sections worldwide (Yan et al., 2009; Zhang et al., 2009; Gorjan et al., 2012; Hammarlund et al., 2012; Jones and Fike, 2013). The global nature of this shift requires a mechanism related to the global sulfur cycle. Earlier studies inferred a shift of the

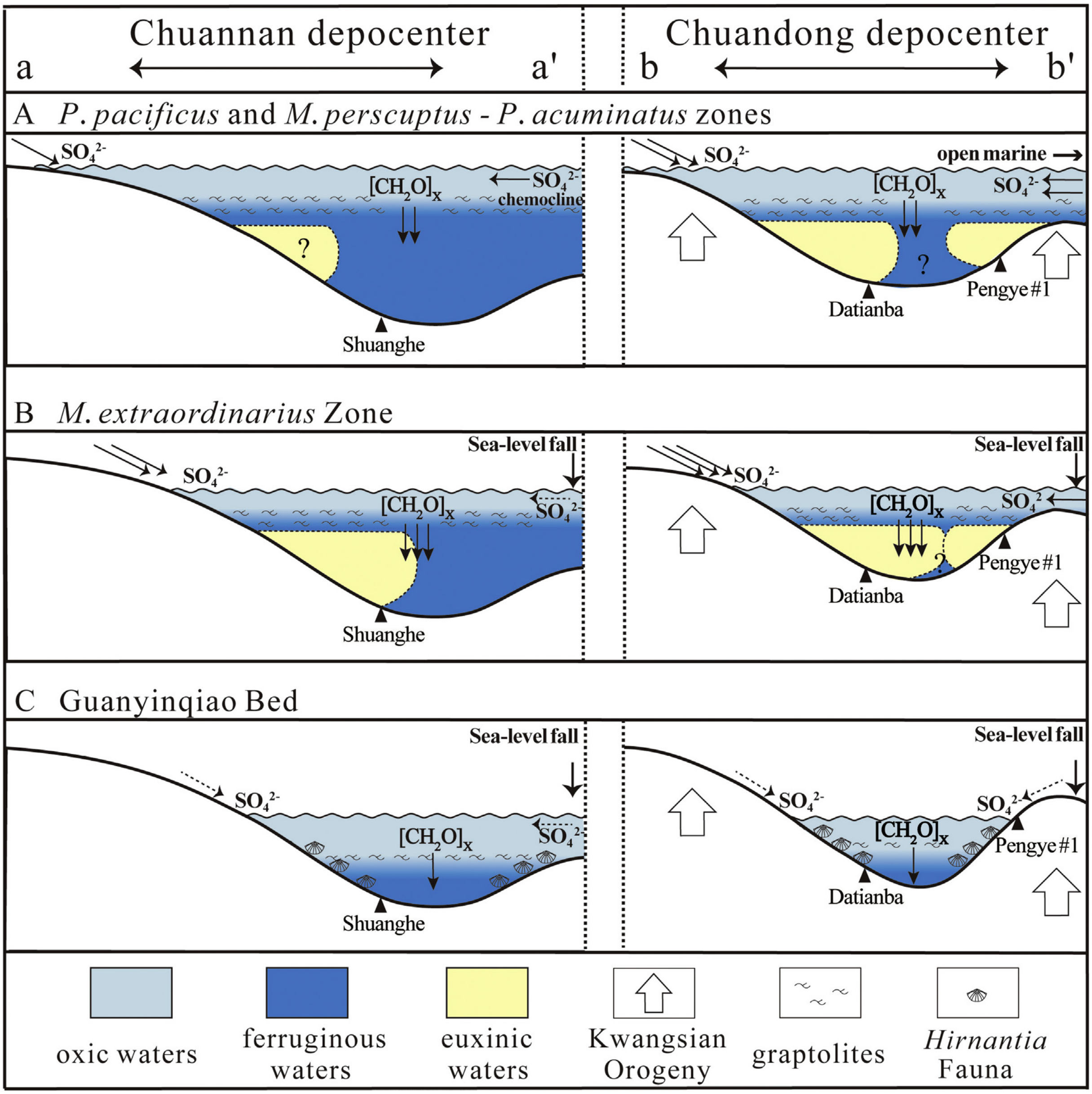

Fig. 8. Depositional model for OST sections in inner Yangtze Sea. (A) *P. pacificus* and *M. persculptus-P. acuminatus* zones (i.e., pre-glacial and post-glacial intervals): locally elevated sulfate fluxes related to tectonic uplifts and open-ocean exchange caused development of euxinia at Pengye #1 and Datianba in the Chuandong depocenter; in contrast, lower sulfate inputs to Chuannan depocenter yielded ferruginous conditions at Shuanghe. (B) *M. extraordinarius* Zone (i.e., early stage of the Hirnantian glaciation): increasing sulfate fluxes resulted in euxinia at all sections because glacio-eustatic fall exposed pyrite-rich shelf sediments to weathering. (C) Guanyinqiao Bed (i.e., the maximum interval of the Hirnantian glaciation): low sulfate fluxes and marine productivity cause the disappearance of euxinia at all sections, possibly as a result of cooler sea-surface temperatures, more limited nutrient supply, and increasing hydrological restriction from the open ocean linked to basin-margin sill shallowing. See text for more details. Directions a-a′ and b-b′ represent the a-a′ and b-b′ transects plotted in Fig. 1C, respectively.

chemocline downward into the sediment as a consequence of glaciation and enhanced oceanic oxygenation, attributing formation of ^{34}S-enriched pyrite to limited sulfate diffusion into sediment porewaters (Yan et al., 2009; Pasquier et al., 2017). However, this mechanism is not fully consistent with our findings of expanded oceanic euxinia in the inner Yangtze Sea during the early Hirnantian. Thus, we infer that this positive $\delta^{34}S_{py}$ shifts observed in study sections represent a consequence of elevated δ^{34}S of seawater sulfate through increased precipitation of ^{32}S-rich pyrite in the restricted inner Yangtze Sea as a result of the Hirnantian glacio-eustatic fall although decreasing S-isotopic fractionation during MSR due to global cooling suggested by Jones and Fike (2013) cannot be excluded. These processes operated concurrently with, and partially counteracted, local additions of ^{32}S-rich sulfate to the inner Yangtze Sea from weathering fluxes, as described above for the *M. extraordinarius* Zone.

7. Conclusions

Our high-resolution chemostratigraphic study of the Pengye #1 section, combined with previously reported data from two other sections representing deeper-water conditions (Shuanghe and Datianba), provides new insights concerning the evolution of euxinic conditions in the inner Yangtze Sea and controls thereon during the Ordovician-Silurian transition (OST). At that time, the inner Yangtze Sea was characterized by a stratified seawater with spatiotemporal redox heterogeneity, substantial but variable hydrological restriction and generally high but spatially variable productivity. Mechanism analyses based on Fe-S-C fluxes show that the development of euxinia in the inner Yangtze Sea, was most likely controlled by local sulfate availability, which varied as a function of both tectonic (Kwangsian Orogeny) and eustatic changes (Hirnantian glaciation). Coexisting S-isotopic record of syngenetic pyrites ($\delta^{34}S_{py}$) demonstrates large differences among study sections, providing evidence for the tectonic and eustatic control on the local sulfate fluxes and in turn euxinic development in the inner Yangtze Sea. Our study highlights potential sulfate control on the development of toxic euxinic waters in those semi-restricted marginal basins and their mechanism links with regional and global events during the OST when the second severest mass extinction of the Phanerozoic occurred.

Acknowledgments

We thank Professors Jiayu Rong, Pingan Peng and anonymous reviewers for their very helpful comments which greatly improved this manuscript. We are also grateful to Dr. Feifei Zhang for editorial handing. We also thank Zihu Zhang, Wei Shi, Biao Chang for laboratory and field assistance, and East China Branch of SINOPEC for sampling permission of Pengye #1 drillcore. This study is funded by the National Natural Science Foundation of China (Grants 41825019 and 41821001), the National Key Research and Development Program of China (Grant 2016YFA0601100), National Natural Science Foundation of China–Research Councils UK–Natural Environment Research Council Program (Grant 41661134048), Strategic Priority Research Program of Chinese Academy of Sciences (Grant XDB26000000) and Fundamental Research Funds for National Universities, China University of Geosciences (Wuhan) (Grant CUGCJ1710).

Appendix A. Supplementary data

Supplementary data to this article can be found online at https://doi.org/10.1016/j.palaeo.2019.109281.

References

Abanda, P.A., Hannigan, R.E., 2006. Effects of diagenesis on trace elements partitioning in shales. Chem. Geol. 230, 42–59. https://doi.org/10.1016/j.chemgeo.2005.11.011.

Algeo, T.J., Ingall, E., 2007. Sedimentary C_{org}: P ratios, paleocean ventilation, and Phanerozoic atmospheric pO_2. Palaeogeogr. Palaeoclimatol. Palaeoecol. 256 (4), 130–155. https://doi.org/10.1016/j.palaeo.2007.02.029.

Algeo, T.J., Lyons, T.W., 2006. Mo-total organic carbon covariation in modern anoxic marine environments: Implications for analysis of paleoredox and paleohydrographic conditions. Paleoceanography 21, PA1016. https://doi.org/10.1029/2004pa001112.

Algeo, T.J., Maynard, J.B., 2004. Trace-element behavior and redox facies in core shales of Upper Pennsylvanian Kansas-type cyclothems. Chem. Geol. 206 (3–4), 289–318. https://doi.org/10.1016/j.chemgeo.2003.12.009.

Algeo, T.J., Rowe, H., 2012. Paleoceanographic applications of trace-metal concentration data. Chem. Geol. 324-325, 6–18. https://doi.org/10.1016/j.chemgeo.2011.09.002.

Algeo, T.J., Lyons, T.W., Blakey, R.C., Over, D.J., 2007. Hydrographic conditions of the Devono-Carboniferous North American Seaway inferred from sedimentary Mo–TOC relationships. Palaeogeogr. Palaeoclimatol. Palaeoecol. 256, 204–230.

Algeo, T.J., Luo, G.M., Song, H.Y., Lyons, T.W., Canfield, D.E., 2015. Reconstruction of secular variation in seawater sulfate concentrations. Biogeosciences 12 (7), 2131–2151. https://doi.org/10.5194/bg-12-2131-2015.

Algeo, T.J., Marenco, P.J., Saltzman, M.R., 2016. Co-evolution of oceans, climate, and the biosphere during the 'Ordovician Revolution': A review. Palaeogeogr. Palaeoclimatol. Palaeoecol. 458, 1–11. https://doi.org/10.1016/j.palaeo.2016.05.015.

Brenchley, P.J., 1988. Environmental changes close to the Ordovician-Silurian boundary. Bulletin of the British Museum of Natural History: Geology 43, 377–385.

Brenchley, P.J., Carden, G.A., Marshall, J.D., 1995. Environmental changes associated with the "first strike" of the Late Ordovician mass extinction. Mod. Geol. 20, 69–82.

Calvert, S.E., 1974. Deposition and diagenesis of silica in marine sediments. In: Hsu, K. (Ed.), Pelagic Sediments: On Land and Under the Sea. 1. Int Assoc. Sediment. Spec. Publ., pp. 273–299. https://doi.org/10.1002/9781444304855.ch12.

Canfield, D.E., 1994. Factors influencing organic carbon preservation in marine sediments. Chem. Geol. 114 (3–4), 315–329. https://doi.org/10.1016/0009-2541(94)90061-2.

Canfield, D.E., Raiswell, R., Westrich, J.T., Reaves, C.M., Berner, R.A., 1986. The use of chromium reduction in the analysis of reduced inorganic sulfur in sediments and shales. Chem. Geol. 54 (1), 149–155. https://doi.org/10.1016/0009-2541(86)90078-1.

Canfield, D.E., Farquhar, J., Zerkle, A.L., 2010. High isotope fractionations during sulfate reduction in a low-sulfate euxinic ocean analog. Geology 38 (5), 415–418. https://doi.org/10.1130/G30723.1.

Charvet, J., Shu, L., Faure, M., Choulet, F., Wang, B., Lu, H., Breton, N.L., 2010. Structural development of the Lower Paleozoic belt of South China: Genesis of an intracontinental orogen. J. Asian Earth Sci. 39 (4), 309–330. https://doi.org/10.1016/j.jseaes.2010.03.006.

Chen, C.(Can), Wang, J.S., Algeo, T.J., Wang, Z., Tu, S., Wang, G.Z., Yang, J.X., 2017. Negative δ^{13}Ccarb shifts in Upper Ordovician (Hirnantian) Guanyinqiao Bed of South China linked to diagenetic carbon fluxes. Palaeogeogr. Palaeoclimatol. Palaeoecol. 487, 430–446.

Chen, C.(Chao), Mu, C., Zhou, K., Liang, W., Ge, X., Wang, X., Wang, Q., Zheng, B., 2016. The geochemical characteristics and factors controlling the organic matter accumulation of the Late Ordovician-Early Silurian black shale in the Upper Yangtze Basin, South China. Mar. Petrol. Geol. 76, 159–175. https://doi.org/10.1016/j.marpetgeo.2016.04.022.

Chen, X., 1984. Influence of the Late Ordovician glaciation on basin configuration of the Yangtze Platform in China. Lethaia 17 (1), 51–59. https://doi.org/10.1111/j.15023931.1984.tb00665.x.

Chen, X., 2012. Onset of the Kwangsian Orogeny as evidenced by biofacies and lithofacies. Sci. China D: Earth Sci. 55 (10), 1592–1600. https://doi.org/10.1007/s11430-012-4490-4.

Chen, X., Rong, J., Li, Y., Boucot, A.J., 2004. Facies patterns and geography of the Yangtze region, South China, through the Ordovician and Silurian transition. Palaeogeogr. Palaeoclimatol. Palaeoecol. 204 (4), 353–372. https://doi.org/10.1016/S0031-0182(03) 00736-3.

Chen, X., Melchin, M.J., Sheets, H.D., Mitchell, C.E., Fan, J.X., 2005. Patterns and processes of latest Ordovician graptolite extinction and recovery based on data from South China. J. Paleontol. 79 (5), 842–861. https://doi.org/10.1666/0022-3360(2005)079[0842:PAPOLO]2.0.CO;2.

Chen, X., Fan, J., Chen, Q., Tang, L., Hou, X., 2014. Toward a stepwise Kwangsian orogeny. Sci. China D: Earth Sci. 57 (3), 379–387. https://doi.org/10.1007/s11430-013-4815-y.

Clarkson, M.O., Poulton, S.W., Guilbaud, R., Wood, R.A., 2014. Assessing the utility of Fe/Al and Fe-speciation to record water column redox conditions in carbonate-rich sediments. Chem. Geol. 382 (11), 111–122. https://doi.org/10.1016/j.chem geo.2014.05.031.

Cocks, L., 2001. Ordovician and Silurian global geography. J. Geol. Soc. Lond. 158, 197–210. https://doi.org/10.1144/jgs.158.2.197.

Cocks, L., Torsvik, T.H., 2002. Earth geography from 500 to 400 million years ago: a faunal and palaeomagnetic review. J. Geol. Soc. Lond. 159 (6), 631–644. https://doi.org/10.1144/0016-764901-118.

Cooper, R.A., Sadler, P.M., Hammer, O., Gradstein, F.M., 2012. The Ordovician Period. In: Gradstein, F.M., Ogg, J.G., Schmitz, M.A., Ogg, G. (Eds.), The Geologic Time Scale 2012. 2. pp. 489–523. https://doi.org/10.1016/B978-0-444-59425-9.00020-2.

Dronov, A., 2013. Late Ordovician cooling event: Evidence from the Siberian Craton. Palaeogeogr. Palaeoclimatol. Palaeoecol. 389 (5), 87–95. https://doi.org/10.1016/j.palaeo.2013.05.032.

Emerson, S.R., Huested, S.S., 1991. Ocean anoxia and the concentrations of molybdenum and vanadium in seawater. Mar. Chem. 34 (3–4), 177–196. https://doi.org/10.1016/0304-4203(91)90002-E.

Erickson, B.E., Helz, G.R., 2000. Molybdenum(VI) speciation in sulfidic waters: Stability and lability of thiomolybdates. Geochim. Cosmochim. Acta 64 (7), 1149–1158. https://doi.org/10.1016/S0016-7037(99)00423-8.

Fan, J., Peng, P., Melchin, M.J., 2009. Carbon isotopes and event stratigraphy near the Ordovician–Silurian boundary, Yichang, South China. Palaeogeogr. Palaeoclimatol. Palaeoecol. 276, 160–169. https://doi.org/10.1016/j.palaeo.2009.03.007.

Fan, J., Melchin, M.J., Chen, X., Wang, Y., Zhang, Y.D., Chen, Q., Chi, Z.L., Chen, F., 2012. Biostratigraphy and geography of the Ordovician-Silurian Lungmachi black shales in South China. Sci. China D: Earth Sci. 54, 1854–1863. https://doi.org/10.1007/s11430-011-4301-3.

Fan, J., Chen, Q., Melchin, M.J., Sheets, H.D., Chen, Z., Zhang, L., Hou, X., 2013. Quantitative stratigraphy of the Wufeng and Lungmachi black shales and graptolite evolution during and after the Late Ordovician mass extinction. Palaeogeogr. Palaeoclimatol. Palaeoecol. 389, 96–114. https://doi.org/10.1016/j.palaeo.2013.08.005.

Faure, M., Shu, L., Wang, B., Charvet, J., Choulet, F., Monie, P., 2009. Intracontinental subduction: a possible mechanism for the Early Palaeozoic Orogen of SE China. Terra Nova 21 (5), 360–368. https://doi.org/10.1111/j.1365-3121.2009.00888.x.

Feng, L., Li, C., Huang, J., Chang, H., Chu, X., 2014. A sulfate control on marine middepth euxinia on the early Cambrian (ca. 529–521 Ma) Yangtze platform, South China. Precambr. Res. 246 (6), 123–133. https://doi.org/10.1016/j.precamres.2014.03.002.

Finnegan, S., Bergmann, K., Eiler, J.M., Jones, D.S., Fike, D.A., Eisenman, I., Hughes, N.C., Tripati, A.K., Fischer, W.W., 2011. The magnitude and duration of Late Ordovician-Early Silurian glaciation. Science 331 (6019), 903–906. https://doi.org/10.1126/science.1200803.

Gibbs, M.T., Kump, L.R., 1994. Global chemical erosion during the Last Glacial Maximum and the present: Sensitivity to changes in lithology and hydrology. Paleoceanography 9 (4), 529–543. https://doi.org/10.1029/94PA01009.

Gill, B.C., Lyons, T.W., Saltzman, M.R., 2007. Parallel, high-resolution carbon and sulfur isotope records of the evolving Paleozoic marine sulfur reservoir. Palaeogeogr. Palaeoclimatol. Palaeoecol. 256 (3), 156–173. https://doi.org/10.1016/j.palaeo.2007.02.030.

Goldhaber, M.B., Kaplan, I.R., 1975. Controls and consequences of sulfate reduction rates in recent marine sediments. Soil Sci. 119 (1), 42–55. https://doi.org/10.1097/00010694-197501000-00008.

Gomes, M.L., Hurtgen, M.T., 2015. Sulfur isotope fractionation in modern euxinic systems: Implications for paleoenvironmental reconstructions of paired sulfate-sulfide isotope records. Geochim. Cosmochim. Acta 157 (5), 39–55. https://doi.org/10.1016/j.gca. 2015.02.031.

Gorjan, P., Kaiho, K., Fike, D.A., Xu, C., 2012. Carbon- and sulfur-isotope geochemistry of the Hirnantian (Late Ordovician) Wangjiawan (Riverside) section, South China: Global correlation and environmental event interpretation. Palaeogeogr. Palaeoclimatol. Palaeoecol. 337-338, 14–22. https://doi.org/10.1016/j.palaeo.2012.03.021.

Habicht, K.S., Gade, M., Thamdrup, B., Berg, P., Canfield, D.E., 2002. Calibration of sulfate levels in the Archean ocean. Science 298 (5602), 2372–2374. https://doi.org/10.1126/science.1078265.

Halevy, I., Peters, S.E., Fischer, W.W., 2012. Sulfate burial constraints on the Phanerozoic sulfur cycle. Science 337 (6092), 331–334. https://doi.org/10.1126/science.1220224.

Hammarlund, E.U., Dahl, T.W., Harper, D.A.T., Bond, D.P.G., Nielsen, A.T., Bjerrum, C.J., Schovsbo, N.H., Schönlaub, H.P., Zalasiewicz, J.A., Canfield, D.E., 2012. A sulfidic driver for the end-Ordovician mass extinction. Earth Planet. Sci. Lett. 331-332 (2), 128–139. https://doi.org/10.1016/j.epsl.2012.02.024.

Helz, G.R., Miller, C.V., Charnock, J.M., Mosselmans, J.F.W., Pattrick, R.A.D., Garner, C.D., Vaughan, D.J., 1996. Mechanism of molybdenum removal from the sea and its concentration in black shales: EXAFS evidence. Geochim. Cosmochim. Acta 60 (19), 3631–3642. https://doi.org/10.1016/0016-7037(96)00195-0.

Helz, G.R., Bura-Nakić, E., Mikac, N., Ciglenečki, I., 2011. New model for molybdenum behavior in euxinic waters. Chem. Geol. 284 (3–4), 323–332. https://doi.org/10.1016/j.chemgeo. 2011.03.012.

Huff, W.D., 2008. Ordovician K-bentonites: issues in interpreting and correlating ancient tephras. Quat. Int. 178, 276–287. https://doi.org/10.1016/j.quaint.2007.04.007.

Ingall, E., Jahnke, R., 1997. Influence of water-column anoxia on the elemental fractionation of carbon and phosphorus during sediment diagenesis. Mar. Geol. 139 (1–4), 219–229. https://doi.org/10.1016/S0025-3227(96)00112-0.

Jablonski, D., 1991. Extinctions: a paleontological perspective. Science 253 (5021), 754. https://doi.org/10.1126/science.253.5021.754.

Jin, C., Li, C., Algeo, T.J., Planavsky, N.J., Cui, H., Yang, X., Zhao, Y., Zhang, X., Xie, S., 2016. A highly redox-heterogeneous ocean in South China during the early Cambrian (529–514 Ma): Implications for biota-environment co-evolution. Earth Planet. Sci. Lett. 441, 38–51. https://doi.org/10.1016/j.epsl.2016.02.019.

Johnston, D.T., Poulton, S.W., Dehler, C., Porter, S., Husson, J., Canfield, D.E., Knoll, A.H., 2010. An emerging picture of Neoproterozoic ocean chemistry: insights from the Chuar Group, Grand Canyon. USA. Earth Planet. Sci. Lett. 290, 64–73. https://doi.org/10.1016/j.epsl.2009.11.059.

Jones, D.S., Fike, D.A., 2013. Dynamic sulfur and carbon cycling through the end-Ordovician extinction revealed by paired sulfate-pyrite δ^{34}S. Earth Planet. Sci. Lett. 363, 144–155. https://doi.org/10.1016/j.epsl.2012.12.015.

Jones, D.S., Martini, A.M., Fike, D.A., Kaiho, K., 2017. A volcanic trigger for the Late Ordovician mass extinction? Mercury data from south China and Laurentia. Geology 45 (7), 631–634. https://doi.org/10.1130/G38940.1.

Kah, L.C., Thompson, C.K., Henderson, M.A., Zhan, R.B., 2016. Behavior of marine sulfur in the Ordovician. Palaeogeogr. Palaeoclimatol. Palaeoecol. 458, 133–153. https://doi.org/10.1016/j.palaeo.2015.12.028.

Khan, M.Z., Feng, Q.L., Zhang, K., Guo, W., 2019. Biogenic silica and organic carbon fluxes provide evidence of enhanced marine productivity in the Upper Ordovician-Lower Silurian of South China. Palaeogeogr. Palaeoclimatol. Palaeoecol (in press).

Kump, L.R., Arthur, M.A., Patzkowsky, M.E., Gibbs, M.T., Pinkus, D.S., Sheehan, P.M., 1999. A weathering hypothesis for glaciation at high atmospheric pCO_2 during the Late Ordovician. Palaeogeogr. Palaeoclimatol. Palaeoecol. 152 (1–2), 173–187. https://doi.org/10.1016/S0031-0182(99)00046-2.

Leavitt, W.D., Halevy, I., Bradley, A.S., Johnston, D.T., 2013. Influence of sulfate reduction rates on the Phanerozoic sulfur isotope record. Proc. Natl. Acad. Sci. (U.S.A.) 110 (28), 11244–11249. https://doi.org/10.1073/pnas.1218874110.

Li, C., Love, G.D., Lyons, T.W., Fike, D.A., Sessions, A.L., Chu, X., 2010. A stratified redox model for the Ediacaran ocean. Science 328, 80–83. https://doi.org/10.1126/science.1182369.

Li, C., Planavsky, N.J., Shi, W., Zhang, Z., Zhou, C., Cheng, M., Tarhan, L.G., Luo, G., Xie, S., 2015. Ediacaran marine redox heterogeneity and early animal ecosystems. Sci. Rep. 5, 17097. https://doi.org/10.1038/srep17097.

Li, J., Yu, B.S., Liu, C., Sun, M.D., 2012. Clay minerals of black shale and their effects on physical properties of shale gas reservoirs in the Southeast of Chongqing: A case study from Lujiao outcrop section in Pengshui, Chongqing. Geoscience 26 (4), 732–740.

Liang, D., Guo, T., Chen, J., Bian, L., Zhao, Z., 2009. Some progresses on studies of hydrocarbon generation and accumulation in marine sedimentary regions, southern China (part 2): geochemical characteristics of four suits of regional marine source rocks. South China. Mar. Origin Petrol. Geol. 14 (1), 1–15.

Little, S.H., Vance, D., Lyons, T.W., McManus, J., 2015. Controls on trace metal authigenic enrichment in reducing sediments: insights from modern oxygen-deficient settings. Am. J. Sci. 315 (2), 77–119. https://doi.org/10.2475/02.2015.01.

Li, Y.F.(Yanfang), Zhang, T., Eills, G.S., Shao, D., 2017a. Depositional environment and organic matter accumulation of Upper Ordovician-Lower Silurian marine shale in the Upper Yangtze Platform, South China. Palaeogeogr. Palaeoclimatol. Palaeoecol. 466, 252–264. https://doi.org/10.1016/j.palaeo.2016.11.037.

Li, Y.F.(Yinfan), Schieber, J., Fan, T.L., Li, Z.Y., Zhang, J.P., 2017b. Regional depositional changes and their controls on carbon and sulfur cycling across the Ordovician-Silurian boundary, northwestern Guizhou, South China. Palaeogeogr. Palaeoclimatol. Palaeoecol. 485, 816–832.

Liu, Y., Li, C., Algeo, T.J., Fan, J., Peng, P., 2016. Global and regional controls on marine redox changes across the Ordovician-Silurian boundary in South China. Palaeogeogr. Palaeoclimatol. Palaeoecol. 463, 180–191. https://doi.org/10.1016/j.palaeo.2016.10.006.

Liu, Z., Algeo, T.J., Guo, X., Fan, J., Du, X., Lu, Y., 2017. Paleo-environmental cyclicity in the Early Silurian Yangtze Sea (South China): tectonic or glacio-eustatic control? Palaeogeogr. Palaeoclimatol. Palaeoecol. 466, 59–76. https://doi.org/10.1016/j.palaeo. 2016.11.007.

Loi, A., Ghienne, J.F., Dabard, M.P., 2010. The Late Ordovician glacio-eustatic record from a high-latitude storm-dominated shelf succession: The Bou Ingarf section (Anti-Atlas, Southern Morocco). Palaeogeogr. Palaeoclimatol. Palaeoecol. 296 (4), 332–358. https://doi.org/10.1016/j.palaeo.2010.01.018.

Lu, X., Kendall, B., Stein, H.J., Li, C., Hannah, J.L., Gordon, G.W., Ebbestad, J.O.R., 2017. Marine redox conditions during deposition of Late Ordovician and Early Silurian organic-rich mudrocks in the Siljan ring district, central Sweden. Chem. Geol. 457, 75–94. https://doi.org/10.1016/j.chemgeo.2017.03.015.

Lyons, T.W., Anbar, A.D., Severmann, S., Scott, C., Gill, B.C., 2009. Tracking euxinia in the ancient ocean: a multiproxy case study. Annu. Rev. Earth Planet. Sci. 379, 161–176. https://doi.org/10.1146/annurev.earth.36.031207.124233.

März, C., Poulton, S.W., Beckmann, B., Küster, K., Wagner, T., Kasten, S., 2008. Redox sensitivity of P cycling during marine black shale formation: Dynamics of sulfidic and anoxic, non-sulfidic bottom waters. Geochim. Cosmochim. Acta 72 (15), 3703–3717. https://doi.org/10.1016/j.gca.2008.04.025.

McManus, J., Berelson, W.M., Klinkhammer, G.P., Hammond, D.E., Holm, C., 2005. Authigenic uranium: relationship to oxygen penetration depth and organic carbon rain. Geochim. Cosmochim. Acta 69 (1), 95–108. https://doi.org/10.1016/j.gca.2004.06.023.

Melchin, M.J., Sadler, P.M., Cramer, B.D., Cooper, R.A., Gradstein, F.M., Hammer, O., 2012. The Silurian Period. In: Gradstein, F.M., Ogg, J.G., Schmitz, M.A., Ogg, G. (Eds.), The Geologic Time Scale 2012. 2. pp. 525–558. https://doi.org/10.1016/B978-0-444-59425-9.00021-4.

Michalopoulos, P., Aller, R.C., 2004. Early diagenesis of biogenic silica in the Amazon delta: alteration, authigenic clay formation, and storage. Geochim. Cosmochim. Acta 68 (5), 1061–1085. https://doi.org/10.1016/j.gca.2003.07.018.

Mort, H.P., Slomp, C.P., Gustafsson, B.G., Andersen, T.R.J., 2010. Phosphorus recycling and burial in Baltic Sea sediments with contrasting redox conditions. Geochim. Cosmochim. Acta 74 (4), 1350–1362. https://doi.org/10.1016/j.gca.2009.11.016.

Mu, E., Li, J., Ge, M., Chen, X., Ni, Y.N., Lin, Y.K., 1981. Paleogeographic maps of the Late Ordovician in the Central China region and their explanation. J. Stratigr. 5, 165–170.

Nie, H.K., Zhang, J.C., Bao, S.J., Bian, R.K., Song, X.J., Liu, J.B., 2012. Shale gas accumulation conditions of the Upper Ordovician-Lower Silurian in Sichuan Basin and its periphery. Oil Gas Geol. 33 (3), 335–344.

Nielsen, J.K., Shen, Y.A., 2004. Evidence for sulfidic deep water during the Late Permian in the East Greenland Basin. Geology 32 (12), 1037–1040. https://doi.org/10.1130/G20987.1.

Pasquier, V., Sansjofre, P., Rabineau, M., Revillon, S., Hough, J., Fike, D., 2017. Pyrite sulfur isotopes reveal glacial-interglacial environmental changes. Proc. Natl. Acad. Sci. (U.S.A.) 114 (23), 5941–5945. https://doi.org/10.1073/pnas.1618245114.

Poulton, S.W., Canfield, D., 2005. Development of a sequential extraction procedure for iron: implications for iron partitioning in continentally derived particulates. Chem. Geol. 214, 209–221. https://doi.org/10.1016/j.chemgeo.2004.09.003.

Poulton, S.W., Canfield, D.E., 2011. Ferruginous conditions: a dominant feature of the ocean through Earth's history. Elements 7 (2), 107–112. https://doi.org/10.2113/gselements.7.2.107.

Poulton, S.W., Raiswell, R., 2002. The low-temperature geochemical cycle of iron: from continental fluxes to marine sediment deposition. Am. J. Sci. 302 (9), 774–805. https://doi.org/10.2475/ajs.302.9.774.

Poulton, S.W., Fralick, P.W., Canfield, D.E., 2004. The transition to a sulphidic ocean ~1.84 billion years ago. Nature 431 (7005), 173–177. https://doi.org/10.1038/nature02912.

Poulton, S.W., Fralick, P.W., Canfield, D.E., 2010. Spatial variability in oceanic redox structure 1.8 billion years ago. Nat. Geosci. 3, 486–490. https://doi.org/10.1038/NGEO889.

Qing, J.Z., Teng, G.E., Yang, Q., Shen, B.J., 2009. Research on maturity indicators of high-maturity marine strata in the eastern Sichuan Basin. Acta Pet. Sin. 30 (2), 208–213.

Ragueneau, O., Tréguer, P., Leynaert, A., Anderson, R.F., Brzezinski, M.A., Demaster, D.J., Dugdale, R.C., Dymond, J., Fischer, G., François, R., 2000. A review of the Si cycle in the modern ocean: recent progress and missing gaps in the application of biogenic opal as a paleoproductivity proxy. Global Planet. Change 26 (4), 317–365. https://doi.org/10.1016/S0921-8181(00)00052-7.

Raiswell, R., Berner, R.A., 1987. Organic carbon losses during burial and thermal maturation of normal marine shales. Geology 15, 853–856.

Raiswell, R., Canfield, D.E., 1998. Sources of iron for pyrite formation in marine sediments. Am. J. Sci. 298 (3), 219–245. https://doi.org/10.2475/ajs.298.3.219.

Raiswell, R., Canfield, D.E., 2012. The iron biogeochemical cycle past and present. Geochem. Perspect. 1 (1), 1–220. https://doi.org/10.7185/geochempersp.1.1.

Raiswell, R., Newton, R., Bottrell, S.H., Coburn, P.M., Briggs, D.E.G., Bond, D.P.G., Poulton, S.W., 2008. Turbidite depositional influences on the diagenesis of Beecher's Trilobite Bed and the Hunsrück Slate; sites of soft tissue pyritization. Am. J. Sci. 308, 105–129. https://doi.org/10.2475/02.2008.01.

Rasmussen, C.M.Ø., Harper, D.A.T., 2011. Interrogation of distributional data for the End Ordovician crisis interval: where did disaster strike? Geol. J. 46, 478–500. https://doi.org/10.1002/gj.1310.

Ries, J.B., Fike, D.A., Pratt, L.M., Lyons, T.W., Grotzinger, J.P., 2009. Superheavy pyrite ($^{34}S_{pyr} > ^{34}S_{CAS}$) in the terminal Proterozoic Nama Group, southern Namibia: A consequence of low seawater sulfate at the dawn of animal life. Geology 37 (8), 743–746. https://doi.org/10.1130/G25775A.1.

Rong, J.Y., 1986. Ecostratigraphy and community analysis of the Late Ordovician and Silurian in Southern China. In: Selected Papers from the 13th and 14th Annual Meetings of Palaeontological Society of China. Anhui Science and Technology

Publishing House, Hefei, China, pp. 1–24.
Rong, J.Y., Zhan, R.B., Harper, D.A.T., 1999. The late Ordovician (Caradoc-Ashgill) Foliomena (Brachiopoda) fauna from China: Implication for its origin, ecological evolution and global distribution. Palaios 14 (5), 412–431. https://doi.org/10.2307/3515394.
Rong, J.Y., Chen, X., Harper, D.A.T., 2002. The latest Ordovician Hirnantia Fauna (Brachiopoda) in time and space. Lethaia 35, 231–249. https://doi.org/10.1111/j.1502-3931.2002.tb00081.x.
Rong, J.Y., Fan, J.X., Miller, A.I., Li, G.X., 2007. Dynamic patterns of latest Proterozoic-Palaeozoic-early Mesozoic marine biodiversity in South China. Geol. J. 42 (3–4), 431–454. https://doi.org/10.1002/gj.1073.
Rong, J.Y., Chen, X., Wang, Y., Zhan, R.B., Liu, J., Huang, B., Tang, P., Wu, R.C., Wang, G.X., 2011. Northward expansion of Central Guizhou Oldland through the Ordovician and Silurian transition: Evidence and implications. Sci. Sin. Terrae 41, 1407–1415 (in Chinese).
Ross, D.J.K., Bustin, R.M., 2009. Investigating the use of sedimentary geochemical proxies for paleoenvironment interpretation of thermally mature organic-rich strata: Examples from the Devonian–Mississippian shales, Western Canadian Sedimentary Basin. Chem. Geol. 260, 1–19. https://doi.org/10.1016/j.chemgeo.2008.10.027.
Rudnick, R.L., Gao, S., 2003. Composition of the continental crust. In: Rudnick, R.L. (Ed.), The Crust, Treatise on Geochemistry. 3. pp. 1–64. https://doi.org/10.1016/B978-0-08-095975-7. 00301-6.
Saltzman, M.R., Young, S.A., 2005. Long-lived glaciation in the Late Ordovician? Isotopic and sequence-stratigraphic evidence from western Laurentia. Geology 33 (2), 109–112. https://doi.org/10.1130/G21219.1.
Schoepfer, S.D., Shen, J., Wei, H., Tyson, R.V., Ingall, E., Algeo, T.J., 2015. Total organic carbon, organic phosphorus, and biogenic barium fluxes as proxies for paleomarine productivity. Earth-Sci. Rev. 149, 23–52. https://doi.org/10.1016/j.earscire v. 2014.08.017.
Scott, C., Lyons, T.W., 2012. Contrasting molybdenum cycling and isotopic properties in euxinic versus non-euxinic sediments and sedimentary rocks: refining the paleoproxies. Chem. Geol. 324, 19–27. https://doi.org/10.1016/j.chemgeo.2012.05.012.
Scott, C., Lyons, T.W., Bekker, A., Shen, Y., Poulton, S.W., Chu, X., Anbar, A.D., 2008. Tracking the stepwise oxygenation of the Proterozoic ocean. Nature 452 (7186), 456–459. https://doi.org/10.1038/nature06811.
Sheehan, P.M., 2001. The late Ordovician mass extinction. Annu. Rev. Earth Planet. Sci. 29 (29), 331–364. https://doi.org/10.1146/annurev.earth.29.1.331.
Shen, J., Schoepfer, S.D., Feng, Q., Zhou, L., Yu, J., Song, H., Wei, H., Algeo, T.J., 2015. Marine productivity changes during the end-Permian crisis and Early Triassic recovery. Earth-Sci. Rev. 149, 136–162. https://doi.org/10.1016/j.earscirev.2014.11.002.
Shen, B., Yang, Y., Teng, G., Qing, J., Pan, A., 2016a. Characteristics and hydrocarbon significance of organic matter in shale from the Jiaoshiba structure, Sichuan Basin: A case study of the Wufeng-Longmaxi formations in well Jianye1. Petrol. Geol. Experiment 38 (4), 480–489.
Shen, J., Feng, Q.L., Algeo, T.J., Li, C., Planavsky, N.J., Zhou, L., Zhang, M.L., 2016b. Two pulses of oceanic environmental disturbance during the Permian-Triassic boundary crisis. Earth Planet. Sci. Lett. 443, 139–152.
Shen, J., Algeo, T.J., Chen, J.B., Planavsky, N.J., Feng, Q.L., Yu, J.X., Liu, J.L., 2019. Mercury in marine Ordovician-Silurian boundary sections of South China is sulfide-hosted and non-volcanic in origin. Earth Planet. Sci. Lett. 511, 130–140.
Stanley, S.M., 2010. Thermal barriers and the fate of perched faunas. Geology 38 (1), 31–34. https://doi.org/10.1130/G30295.1.
Su, W., Huff, W.D., Ettensohn, F.R., Liu, X., Zhang, J., Li, Z., 2009. K-bentonite, black-shale and flysch successions at the Ordovician-Silurian transition, South China: Possible sedimentary responses to the accretion of Cathaysia to the Yangtze Block and its implications for the evolution of Gondwana. Gondwana Res. 15, 111–130. https://doi.org/10.1016/j.gr.2008.06.004.
Thompson, C.K., Kah, L.C., 2012. Sulfur isotope evidence for widespread euxinia and a fluctuating oxycline in Early to Middle Ordovician greenhouse oceans. Palaeogeogr. Palaeoclimatol. Palaeoecol. 313-314, 189–214. https://doi.org/10.1016/j.palaeo.2011.10.020.
Tribovillard, N., Riboulleau, A., Lyons, T., Baudin, F.O., 2004. Enhanced trapping of molybdenum by sulfurized marine organic matter of marine origin in Mesozoic limestones and shales. Chem. Geol. 213 (4), 385–401. https://doi.org/10.1016/j.chemg eo. 2004.08.011.
Tribovillard, N., Algeo, T.J., Lyons, T., Riboulleau, A., 2006. Trace metals as paleoredox and paleoproductivity proxies: an update. Chem. Geol. 232 (1–2), 12–32. https://doi.org/10.1016/j.chemgeo.2006.02.012.
Wang, H.Z., 1985. Atlas of the Palaeogeography of China. Cartographic Publishing House, Beijing.
Wang, G.X., Zhan, R.B., Percival, I.G., 2019. The end-Ordovician mass extinction: A single-pulse event? Earth-Sci. Rev. 192, 15–23.
Wanty, R.B., Goldhaber, M.B., 1992. Thermodynamics and kinetics of reactions involving vanadium in natural systems: accumulation of vanadium in sedimentary rocks. Geochim. Cosmochim. Acta 56, 1471–1483. https://doi.org/10.1016/0016-7037(92)90217-7.
de Wever, P., Dumitrica, P., Caulet, J.P., Nigrini, C., Caridroit, M., 2001. Radiolarians in the Sedimentary Record. Gordon and Breach Science Publishers, Singapore 525 pp.
Wignall, P.B., Newton, R., 1998. Pyrite framboid diameter as a measure of oxygen deficiency in ancient mudrocks. Am. J. Sci. 298 (7), 537–552. https://doi.org/10.2475/ajs.298.7.537.
Wilkin, R.T., Barnes, H.L., 1997. Formation processes of framboidal pyrite. Geochim. Cosmochim. Acta 61 (2), 323–339. https://doi.org/10.1016/S0016-7037(96)00320-1.
Wilkin, R.T., Barnes, H.L., Brantley, S.L., 1996. The size distribution of framboidal pyrite in modern sediments: an indicator of redox conditions. Geochim. Cosmochim. Acta 60 (20), 3897–3912. https://doi.org/10.1016/0016-7037(96)00209-8.
Yan, D., Chen, D., Wang, Q., Wang, J., Wang, Z., 2009. Carbon and sulfur isotopic anomalies across the Ordovician-Silurian boundary on the Yangtze Platform, South China. Palaeogeogr. Palaeoclimatol. Palaeoecol. 274 (1–2), 32–39. https://doi.org/10.1016/j.palaeo. 2008.12.016.
Yan, D., Chen, D., Wang, Q., Wang, J., 2010. Large-scale climatic fluctuations in the latest Ordovician on the Yangtze block, south China. Geology 38 (7), 599–602. https://doi.org/10.1130/G30961.1.
Yan, D., Chen, D., Wang, Q., Wang, J., 2012. Predominance of stratified anoxic Yangtze Sea interrupted by short-term oxygenation during the Ordo-Silurian transition. Chem. Geol. 291 (1), 69–78. https://doi.org/10.1016/j.chemgeo.2011.09.015.
Yang, S., Hu, W., Wang, X., Jiang, B., Yao, S., Sun, F., Huang, Z., Zhu, F., 2019. Duration, evolution, and implications of volcanic activity across the Ordovician-Silurian transition in the Lower Yangtze region. South China. Earth Planet. Sci. Lett. 518, 13–25.
Young, S.A., Gill, B.C., Edwards, C.T., Saltzman, M.R., Leslie, S.A., 2016. Middle–Late Ordovician (Darriwilian–Sandbian) decoupling of global sulfur and carbon cycles: isotopic evidence from eastern and southern Laurentia. Palaeogeogr. Palaeoclimatol. Palaeoecol. 458, 118–132. https://doi.org/10.1016/j.palaeo.2015.09.040.
Zhan, R., Liu, J., Percival, I.G., Jin, J., Li, G., 2010. Biodiversification of Late Ordovician Hirnantia fauna on the Upper Yangtze Platform, South China. Sci. China D: Earth Sci. 53 (12), 1800–1810. https://doi.org/10.1007/s11430-010-4071-3.
Zhang, T.G., Shen, Y., Zhan, R., Shen, S., Chen, X., 2009. Large perturbations of the carbon and sulfur cycle associated with the Late Ordovician mass extinction in South China. Geology 37 (4), 299–302. https://doi.org/10.1130/G25477A.1.
Zhang, X.L., Li, Y., Lu, H., Yan, J., Tuo, J., Zhang, T., 2013. Relationship between organic matter characteristics and depositional environment in the Silurian Longmaxi Formation in Sichuan Basin. J. China Coal Soc. 38 (5), 851–860.
Zhang, J.K., He, S., Yi, J.Z., Zhang, B.J., Zhang, S.W., Zheng, L.J., Hou, Y.G., Wang, Y., 2014a. Rock thermos-acoustic emission and basin model technologies applied to the study of maximum paleotemperatures and thermal maturity histories of Lower Paleozoic marine shales in the western middle Yangtze area. Acta Pet. Sin. 35 (1), 58–67. https://doi.org/10.7623/syxb201401006.
Zhang, L., Fan, J., Chen, Q., Wu, S., 2014b. Reconstruction of the mid-Hirnantian palaeotopography in the Upper Yangtze region, South China. Est. J. Earth Sci. 63 (4), 329. https://doi.org/10.3176/earth.2014.39.
Zhang, L., Fan, J., Chen, Q., 2016. Geographic distribution and palaeogeographic reconstruction of the Upper Ordovician Kuanyinchiao Bed in South China. Chin. Sci. Bull. 61, 2053–2063 (in Chinese).
Zhang, J.P., Fan, T.L., Zhang, Y.D., Lash, G.G., Li, Y.F., Wu, Y., 2017. Heterogenous oceanic redox conditions through the Ediacaran-Cambrian boundary limited the metazoan zonation. Sci. Rep. 7 (1), 8550. https://doi.org/10.1038/s41598-017-07904-3.
Zheng, Y., Anderson, R.F., Geen, A.V., Kuwabara, J., 2000. Authigenic molybdenum formation in marine sediments: a link to pore water sulfide in the Santa Barbara Basin. Geochim. Cosmochim. Acta 64 (24), 4165–4178. https://doi.org/10.1016/S0016-7037(00)00495-6.
Zhou, L., Algeo, T.J., Shen, J., Hu, Z., Gong, H., Xie, S., Huang, J., Gao, S., 2015. Changes in marine productivity and redox conditions during the Late Ordovician Hirnantian glaciation. Palaeogeogr. Palaeoclimatol. Palaeoecol. 420, 223–234. https://doi.org/10.1016/j.palaeo.2014.12.012.
Zou, C.N., Qiu, Z., Wei, H., Dong, D., Lu, B., 2017. Euxinia caused the Late Ordovician extinction: Evidence from pyrite morphology and pyritic sulfur isotopic composition in the Yangtze area, South China. Palaeogeogr. Palaeoclimatol. Palaeoecol. 511, 1–11. https://doi.org/10.1016/j.palaeo.2017.11.033.